ORIGINAL ARTICLE

Adsorptive behaviour of rutile phased titania nanoparticles supported on acid-modified kaolinite clay for the removal of selected heavy metal ions from mining wastewater

Mary Adejoke Ajala[1,3,4] · Ambali Saka Abdulkareem[1,3] · Jimoh Oladejo Tijani[2,3] · Abdulsalami Sanni Kovo[1,3]

Abstract

This study investigated the removal of metal ions pollutants in mining wastewater such as Mn (II), Fe (III), Pb (II) and Cu (II) ions by acid-activated kaolinite clay (AAC) and titanium (IV) oxide (TiO_2) nanoparticles supported on the AAC (TiO_2–AAC). TiO_2 nanoparticles were synthesised using titanium salt precursor with leaves extract of *Parkia biglobossa* and impregnated on the AAC to develop TiO_2-AAC as a nanoadsorbent. The AAC and TiO_2–AAC nanocomposites were characterized using different analytical techniques. Actual concentrations of selected heavy metals in mining wastewater was determined prior and after treatment using the prepared adsorbents in batch adsorptive studies with atomic absorption spectrophometer. The characterisation studies confirmed that a rutile phase TiO_2 was doped the on acid-activated kaolinite clay. Morphology analysis shows that the developed adsorbents were homogeneously dispersed and porous. The results of the surface area further revealed that the AAC, TiO_2 and TiO_2–AAC has 14.15, 10.23 and 32.98 m^2/g, respectively. The percentage removal of heavy metals followed the order of TiO_2–AAC > AAC due to the higher surface area and enhanced surface functionality of the former than the latter. The adsorption capacity increased from 86.13 to 91.99% (Fe (III)), 83.12 to 89.37% (Mn (II)), 68.48 to 81.95% (Cu (II)) and 29.49 to 32.39% (Pb (II)) from AAC to TiO_2–AAC. The kinetic and isotherm models were best fitted by pseudo-second-order kinetics and Langmuir model. Whilst the thermodynamic investigation found that, the adsorption process was endothermic, spontaneous and chemisorption controlled. Conclusively, the TiO_2–AAC nanocomposite exhibited better performance than AAC alone.

Keywords Mine site · Manganese · Lead · Titanium (IV) oxide · Isotherm · Kinetics · Adsorption technology

Introduction

The challenges posed by urbanisation and industrialisation are humongous. Among these is water pollution, which endangers the survival of both plants and animals in the present twenty-first century due to exposure to different contaminants. Toxic pollutants of several types are being released into the water bodies causing considerable damages to the human organs, plants and distortion of the ecosystem (Manisalidis et al. 2020; Redha et al. 2021). These pollutants are released as by-products from the operations of metallurgy, electroplating, painting, pharmaceutical and mining industries (Wang et al. 2021). Mining, as an economic activity has contributed greatly to the GDP growth of several countries (Acheampong and Ansa 2017; Wang et al. 2021) however there is an attendant challenge of pollution especially the release of wastewater containing heavy metals causing severe damage to the water resources (Saha and Sinha 2018). Heavy metals which includes Mn, Pb, Ni, Fe, Cu, Cd, Cr with other physicochemical parameters like; turbidity, sulphate, phosphate, nitrate, COD, BOD are the major characteristics of an abandoned mining site wastewater (Bwapa et al. 2017; Ojonimi et al. 2019). Exposure to

✉ Mary Adejoke Ajala
  ajala.ma@unilorin.edu.ng

1   Department of Chemical Engineering, Federal University of Technology, Minna, Niger State, Nigeria

2   Department of Chemistry, Federal University of Technology, Minna, Niger State, Nigeria

3   Nanotechnology Research Group, Centre for Genetic Engineering and Biotechnology (CGEB), Federal University of Technology, Niger State, P.M.B 65, Minna, Niger State, Nigeria

4   Department of Chemical Engineering, University of Ilorin, Ilorin, Kwara State, Nigeria

these contaminants is the major cause of infirmities, diseases and dysfunctions both in plants and animals (Balali-Mood et al. 2021). Lead (Pb) as a heavy metal has been reported to cause mental retardation, hyperactivity, kidney damage, dermatitis, encephalopathy and cardiovascular dysfunctions (Balali-Mood et al. 2021). Exposure to Cd causes lungs cancer and birth defects (Wang et al. 2021). Chromium exposure can cause skin epidemics, respiratory complications, severe renal failure, debilitated immune systems, kidney and liver impairment, alteration of genetic material, lung cancer, respiratory fibrosis (Pavesi and Moreira 2020). Nickel can also cause lungs, nose and bone cancer, dizziness, headache, queasiness and vomiting, chest pain, rapid respiration (Lakherwal 2014). Other effect includes: liver cirrhosis, thyroid dysfunction, skin peels, diarrhoea, stunted growth, lower reproduction rate, bioaccumulation in food chain, death of organisms and distortion of the ecosystem (Balali-Mood et al. 2021; Wang et al. 2021). Thus, there is urgent need to treat mining wastewater prior to release into the environment.

Conventional wastewater treatment techniques such as filtration (Bhateria and Singh 2019), chemical oxidation (Oh et al. 2020), ion exchange (Zhao et al. 2019), ozonation (Prasse et al. 2015), flocculation, electro-coagulation (Fu et al. 2019), reverse osmosis, electrodialysis, precipitation, co-precipitation flocculation, (Bijang et al. 2020) have been employed to treat complex industrial wastewater such as mining wastewater. These techniques have certain limitations such as the high cost of reagents, generation of toxic sludge, high post-treatment cost, occupation of space, high energy requirements, and failure to remove heavy metals in the range of 1–100 mg/L amongst others (Gholipour et al. 2020). On the contrary, adsorption technology shows exceptional characteristics such as simplicity in design, cost-effectiveness, eco-friendly and high removal efficiency especially when heavy metals concentration in wastewater ranges from 1 to 100 mg/L (Yang et al. 2019; Subhi et al. 2020).

Several adsorbents like activated carbon (Egbosiuba et al. 2019; Shukla et al. 2020), date seed activated carbon: (Subhi et al. 2020), Turmeric/polyvinyl alcohol Th(IV) phosphate electrospun fibers (Ahamed et al. 2016), clays, zeolites, alumina, polymeric materials (Ahamed et al. 2016; Khan et al. 2019; Pietrelli et al. 2019) and nanomaterials have been used by diverse researchers to impound heavy metals from wastewater (Siddiqui and Chaudhry 2017). Amongst nanomaterials widely employed for environmental remediation are metallic and metal oxide nanoparticles like titanium dioxide, zinc oxide, tungsten oxide, iron oxide, silicon oxide nanoparticles to mention but a few (Guillaume et al. 2018; Guo et al. 2013; Liu et al. 2015; Yang et al. 2019). TiO_2 nanoparticles are widely investigated by researchers due to their photochemical, thermal and biological stability, low cost, low toxicity, great refractive index, excellent antimicrobial

and adsorptive properties amongst others (Durango-Giraldo et al. 2019; Landage et al. 2020). Titanium (IV) oxide exists as anatase, brookite or in the rutile phase with the anatase phase unstable and most suitable for photocatalytic applications (Musial et al. 2020; Tijani et al. 2019). Studies have shown that most biological synthesised TiO_2 are anatase phase or mixed TiO_2 phases and are commonly used for photocatalytic applications (Krishnan and Mahalingam 2017; Mustapha et al. 2020) while TiO_2 in the rutile phase is employed as an adsorbent because of thermal stability and presence of more anchoring sites to sequester adsorbate in the aqueous medium. Rutile TiO_2 has also been reported to have reduction kinetics of 2.5 times faster than anatase TiO_2, depicting an improved activity (Oi et al. 2016). Despite the advantages of TiO_2 nanoparticles, it agglomerates when dispersed in aqueous medium, this affects its surface area and pose challenges to recover due to the nanocrystalline size, which seriously limits its practical application (Akinnawo 2019). To prevent the agglomeration, improve post-separation from wastewater and ensure the stability of TiO_2 nanoparticles, modification by a metal–organic framework, functionalization based on doping mechanism, on supports materials have been identified as a viable alternative (Falk et al. 2018; Madadi et al. 2020; Rodríguez-Padrón et al. 2019). Materials such as MgO, Al_2O_3, graphite, zeolite, carbon nanotubes, furacene and clay have been used to support TiO_2 and other metal oxides to solve post-separation problems (Khan et al. 2019; Krishnan and Mahalingam 2017; Ouyang et al. 2019; Youssef et al. 2015). Kaolinite clay have efficient removal capacity aimed at heavy metal ions through the ion exchange process (Mustapha et al. 2019). To achieve this, the unwanted metal ions become confined to the clay through, electrostatic force of attraction amid the metal ions in solution and the anionic surfaces on the clay particles in the adsorption process (Abdallah 2019). Other desirable properties of kaolinite clay in adsorption are; cation exchange ability, non-toxicity, cheap costs, eco-friendly and availability.

Kaolinite clays have been used for wastewater treatment especially, metal ion removal in aqueous wastewaters. Saudi natural clay was applied for Ni and Cd adsorption from an aqueous solution and the research established the efficiency of the clay for adsorption applications (Khan et al. 2019). Clay without modification was also used for successful adsorption of Cu and Pb from simulated wastewater (Budsaereechai et al. 2012). Modified and unmodified kaolinite clay was used by Al-Essa and Khalili (2018) for treating wastewater. Mungondori et al. (2017) made use of clay composite without chemical modification for the removal of selected heavy metal ions from simulated wastewater. In addition, TiO_2, TiO_2/SiO, $TiO_2/bentonite$ clay was also used for the removal of pollutants in wastewater but, most of these adsorbents were unmodified with acid and the obtained

phase of TiO$_2$ not rutile phase of titania (Ashraf et al. 2019; Cardoso et al. 2019; Krishnan and Mahalingam 2017). There is therefore, paucity of information on the use of green synthesised rutile titanium (IV) oxide nanoparticle supported on acid activated clay for the removal of heavy metal from mine site wastewater. The present study, hitherto, focused on the green synthesis of rutile-phase titanium nanoparticles using *Parkia biglobossa* leaves extract, immobilised on acid activated kaolinite clay for the comparative adsorption studies of selected heavy metals from deleterious mining wastewater onto the activated clay (AAC) and titanium (IV) oxide immobilised on activated clay (TiO$_2$–AAC).

Materials and method

Titanium (IV) isopropoxide, sodium hydroxide, hydrochloric acid and tetra Oxo sulphate (IV) acid having percentage purity in the range of 95–99.8% were obtained from Sigma-Aldrich. The chemicals used were of analytical grade and used as received without further purification.

The fresh leaves of Locust bean (*Parkia biglobossa*) were obtained from different locations in Ilorin, Kwara State (Nigeria) Metropolis. A plant Taxonomist at the department of Plant Biology, University of Ilorin, Ilorin, Kwara State, Nigeria, identified the leaves. Local clay was collected from clay deposits in Akerebiata, Ilorin, while mining wastewater was collected from the *Chanchaga, Chanchaga* Local government Area, Minna, Niger State, Nigeria.

Pre-treatment and preparation of plant extract

The locust bean leaves were washed with distilled water, dried at ambient temperature in the laboratory for 14 days. To prepare the plant extract, 5 g of the pulverised leaves were weighed into a 250 mL beaker, followed by the addition of 0.1 L of deionised water. The mixture was stirred and heated at 70 °C for 15 min using a magnetic stirrer, and later allowed to cool to room temperature. Then, filtered using Whatman No. 1 filter paper and the filtrate (aqueous leaves extract) was stored in a refrigerator at 4 °C.

Beneficiation and Acid activation of nanoclay

The raw clay was beneficiated by sedimentation technique to obtain a fraction of < 300 mm particle size. This was done by weighing 250 g of milled clay sample in a petri dish; the weighed clay was dispersed into containers containing 5000 mL of distilled water and stirred. The mixture was allowed to stay for 24 h for proper intercalation of the clay structure by water molecules, then sieved with a 300 mm sieve diameter. The sieved clay was allowed to settle in

containers and the settling time of the clay was obtained using the Eq. (1).

$$r^2 = \frac{9\mu h}{2(\rho_1 - \rho_2)gt} \tag{1}$$

where r = particle size (radius) of clay, assumed to be spherical, μ = viscosity of distilled water, h = settling height of fluid, g = gravitational acceleration, ρ_1 = clay density, ρ_2 = water density, and t = settling time

The settled clay was decanted, sun-dried and dried in the oven at 100 °C for 1 h to obtain a constant weight. The dried clay was pulverised with an industrial pulveriser, then sieved with 250 mm diameter sieve, to obtain beneficiated clay.

Acid-activation of beneficiated kaolinite clay

The acid activation of beneficiated kaolinite clay was carried out as follows: 50 g of beneficiated clay was weighed into a 500 mL beaker, followed by the addition of 150 mL of de-ionised water. The mixture was stirred to form a homogeneous solution and 100 mL of 98% concentrated H$_2$SO$_4$ was added and stirred at 200 rpm for 2 h to prevent the content from forming mud. Thereafter, the slurry was allowed to age for 3 h; then washed severally with de-ionised water until a pH of 7 was attained and subsequently filtered. The sediment was oven-dried at 100 °C for 2 h to remove residual water and then pulverised, then coded as AAC and kept in a sample bottle.

Green synthesis of titanium (IV) oxide nanoparticles

The synthesis of TiO$_2$ nanoparticles was carried out using the modified method described by Tijani et al. (2019) and Zahir et al. (2015). A known volume (50 cm^3) of *Parkia biglobossa* aqueous leaves extract was measured into a 250 mL beaker followed by slowed addition of 50 cm^3 of 0.1 M titanium (IV) isopropoxide under continuous stirring on a magnetic stirrer at 2000 rpm for 2 h. The pH of the mixture was adjusted to 8 using 1 M NaOH solution. The colour changed was accompanied with the formation of precipitates. The TiO$_2$ nanoparticles formed were filtered, washed severally with distilled water and allowed to age overnight. The TiO$_2$ cake was oven-dried at 70 °C for 1 h followed by calcination in a muffle furnace at 550 °C for 2 h.

Preparation of Titanium (IV) oxide doped acid-activated kaolinite clay nanocomposite

TiO$_2$/activated kaolinite clay nanocomposites were prepared by wet impregnation method: 2.5 g of the TiO$_2$ nanoparticles prepared were dispersed in 50 mL of distilled water and 20 g of activated kaolinite clay was added, the mixture was stirred

at 200 rpm for 2 h. The resulting slurry was allowed to age for 12 h, oven dried at 70 °C for 2 h and then calcined in a muffle furnace at 550 °C for 2 h and the powdered titanium (IV) oxide supported activated clay nanocomposite obtained was coded (TiO$_2$–AAC).

Characterisation of the synthesised titanium dioxide

The UV–Visible absorption spectrophotometry analysis was done to determine the absorption wavelength of the TiO$_2$ nanoparticles using the UV-SPECTROMETER, (UV-1800, SHIMADZU, Japan). The crystal composition/phase of the titanium (IV) oxide-based material was determined by X-ray diffraction (Bruker AXS D8 X-Ray Machine with CuKα radiation) and the crystallite size calculated using the Scherer equation (Eq. 2).

$$D = \frac{K\lambda}{B\mathrm{Cos}\theta} \tag{2}$$

where λ = wavelength of X-ray.
K = Scherer's constant (0.9).
B = Full Width at Half maximum (FWHM).
θ = diffraction angle.
D = Average crystallite size.

The functional groups in the materials were identified using Perkin Elmer 100 FT-IR spectrometer model "two". High-resolution scanning electron microscopy (Zeiss Auriga HRSEM) was used for the determination of the morphology of the particles. The surface area and pore size and pore volume of the samples were determined using the Brunauer, Emmet and Teller (BET) Nitrogen adsorption procedure on NOVA 4200e model equipment. The samples were degassed at 200 °C for 2 h under inert nitrogen gas flow, to remove adsorbed moisture and organic compounds that may block the pores. While X-ray photoelectroscopy (XPS) model (PHI 5400 XPS spectrometer); with a non-monochromatic (Mg Kα) X-ray source was used to determine the surface oxidation states of the elements in the composite materials.

Batch adsorption behaviour of AAC and TiO$_2$-AAC

The batch adsorption experiments for the removal of Mn (II), Fe (III), Pb (II) and Cu (II) ions from mining wastewater onto activated kaolinite clay (AAC) and activated kaolinite clay-TiO$_2$ (AAC–TiO$_2$) were performed based on the variation of contact time (20–180 min), adsorbent dose (0.1–1.0 g), and temperature (30–70 °C). A thermostatic water bath shaker (Pye Unicam SP-9 Cambridge, UK) was utilised to carry out the adsorption experiments and the stirring speed was maintained at 200 rpm for all experiments. The effect of each parameter on the removal efficiency of the

selected heavy metals from mining wastewater is described as follows.

Effect of contact time

The effect of contact time on the rate of removal of Mn (II), Fe (III), Pb (II) and Cu (II) by the AAC and AAC-TiO$_2$ can be described as follows: 100 cm^3 of mining wastewater was measured into a 200 mL conical flask, 0.5 g each of AAC and TiO$_2$-AAC was weighed and added into the wastewater. The flasks were prepared in duplicates, covered and then placed in the thermostatic water bath shaker maintained at 30 °C and 200 rpm for the diverse contact times (20, 40, 60, 80, 100, 120, 140, 160 and 180 min). After each contact time, the samples were withdrawn from the flask, filtered and the filtrate was analysed using Atomic Absorption Spectrophotometer (AAS) (PG990 model). The quantity of each of the metal ion adsorbed was calculated using Eq. (3), adsorption at equilibrium was calculated using Eq. (4) while the percentage removal was calculated with Eq. (5).

Effect of adsorbent dosage

The influence of adsorbent dosage on the removal efficiency of Mn (II), Fe (III), Pb (II) and Cu (II) from mining wastewater was determined by the addition of varied quantities of the activated clay and (0.1, 0.2, 0.3, 0.4, 0.5, 0.6, 0.7, 0.8, 0.9 and 1.0 g) into 0.1 L of the mining wastewater in a 200 mL conical flask. The covered flask was placed in the thermostatic water bath shaker set at 30°C while sustaining a constant contact time (120 min). After 120 min of the adsorbate interaction with the adsorbent, the solution was filtered and the filtrate was analysed with the AAS. The amount of each metal ion removed was also calculated using Eq. (5).

Effect of temperature

The temperature influence on the heavy metal ions adsorbed was investigated by adding 0.5 g of the adsorbent to 0.1 L of the mining wastewater in a 200 mL conical flask. The flasks were made in duplicates, then placed in the thermostatic water bath shaker. The flasks were carefully covered and the temperature varied to 30, 40, 50, 60 and 70°C using equilibrium contact time (120 min). Sampling was done at the end of 120 min, followed by filtration using Whatman No. 1. Filter paper. Then, the filtrates were examined for the selected heavy metals using AAS.

pH point of zero charges (pH$_{PZC}$) determination for AAC and AAC–TiO$_2$

The pH point of zero charges (pHPZC) of the two materials, which is conveyed as the electrical balance between

the adsorbent surface and metal ion adsorbate solution was determined. 0.1 L of mining wastewater was measured into 12 separate Erlenmeyer flasks (in duplicates), the initial pH (pH$_i$) was measured in the range of 2–12 (at 2.0 intervals) for the different flasks. Few drops of 2.0 M of HCl or NaOH was added to the mixture to control the pH of the solution using a pH meter (Eutech Instruments, Model Ecoscan Singapore). The determined optimum dosage (5 g) of AAC and TiO$_2$–AAC was added into 12 flasks separately, afterwards arranged on a shaker for 48 h in order to achieve balance charges between the surface of the adsorbent and the wastewater. The suspension was filtered after 48 h and the final pH at equilibrium (pH$_f$) of the filtrate was recorded. The pH$_{PZC}$ of each adsorbent represents the meeting point between the pH$_i$ curve against pH$_f$ curve. The technique was repeated for AAC to determine its point of zero pH charge as well.

Data analysis

The amount of each metal ion (Mn (II), Fe (III), Pb (II) and Cu (II)) adsorbed at equilibrium was calculated by using Eq. 3:

$$q_t = \frac{(C_o - C_t)V}{m} \tag{3}$$

While, the adsorption at equilibrium, q_e(mg/g), was analysed using Eq. 4:

$$q_e = \frac{(C_o - C_e)V}{m} \tag{4}$$

And the percentage of metal ion removal was calculated using Eq. 5 (Guillaume et al. 2018):

$$\text{Removal (\%)} = \frac{C_o - C_t}{C_o} \times 100\% \tag{5}$$

where C_o is the initial concentration, C_t is concentration at time t, and C_e is the equilibrium metal ion concentration (mg/L) respectively. V represents the water sample volume (L), m is the mass (g) of adsorbent used and $q_{e,t}$ (mg/g) is the adsorption capacity of metal ion adsorbed per gram of the adsorbent at equilibrium.

Kinetic study

The adsorption kinetics of (Mn), Iron (Fe), Lead (Pb) and Copper (Cu) metal ions onto AAC and AAC–TiO$_2$, were analysed using four kinetic models namely; pseudo-first-order (PFO) (Miyah et al., 2017), pseudo-second-order (PSO) (Ho and McKay, 1999), intraparticle diffusion and Elovich kinetic model (Boparai et al., 2011). The PFO model is expressed mathematically as shown in Eq. 6:

$$\ln(q_e - q_t) = q_e - k_1 t \tag{6}$$

The PSO model is shown in Eq. 7:

$$\frac{dq_t}{dt} = k_2(q_e - q_t)^2 \tag{7}$$

Also, q_e (mg/g) is the adsorption capacity of metal ion adsorbed per gram of the adsorbent at equilibrium, while q$_t$ is the adsorbed phase at a time, t.

The intraparticle diffusion model is expressed by the relationship presented in Eq. 8:

$$q_t = K_p t^{1/2} + C_p \tag{8}$$

The Elovich kinetic model is as presented in Eq. 9:

$$q_t = \frac{1}{\beta} \ln(\alpha\beta) + \frac{1}{\beta} \ln t \tag{9}$$

where q_e (mg/g) is the adsorbed quantity of metal ion at equilibrium, q_t (mg/g) is the adsorbed amounts of each metal ion at time t (min), k_1 (min^{-1}), k_2 (mg/g min), k_{int} (mg/g min$^{1/2}$) and α (mg/g min) are; pseudo-first order, pseudo-second order, intraparticle diffusion and Elovich rate constants. C (mg/g) equals the constant for the boundary layer thickness, while β (mg/g min) represents the constant for the desorption rate relative to the activation energy for surface coverage extent and chemisorption process.

Adsorption isotherm model

Different adsorption isotherm models were applied to evaluate the distribution of adsorbate molecules at the solid/liquid interface. The equilibrium adsorption data obtained were analysed using Langmuir (Langmuir 1918), Freundlich (Miyah et al. 2017), Temkin (Egbosiuba et al. 2019) and Dubinin–Radushkevich (D–R) (Ayawei et al. 2017; Dubinin 1969) models to show metal ions adsorption onto the surface of the AAC and AAC-TiO$_2$.

The mathematical representation of the Langmuir isotherm model is given by Eq. (9):

$$\frac{C_e}{q_e} = \frac{1}{q_o K_L} + \frac{C_e}{q_o} \tag{10}$$

where q_e (mg/g) is the amount of metal ion uptake at equilibrium, q_m (mg/g) represents maximum adsorption capacity for monolayer coverage on the surface of the adsorbent. C_e (mg/L) represents metal ions concentration at equilibrium while k_L (L/mg) is the Langmuir equilibrium adsorption constant.

Freundlich isotherm model equation is given in Eq. 11:

$$\ln q_e = \ln K_F + \frac{1}{nF} \ln C_e \tag{11}$$

where K_F in mg/g and n_F is the Freundlich adsorption isotherm constant which denotes the adsorption capacity of the AAC and the heterogeneity of the adsorption process, respectively.

Temkin isotherm model equation is presented in Eq. 12:

$$q_e = \frac{RT}{b_T} \ln A_T + \frac{RT}{b_T} \ln C_e \tag{12}$$

where A_T (L/g) and b_T (kJ/mol) are Temkin constants, associated with the heat of adsorption and maximum binding energy. T (ºC) is the temperature, while R (8.314 J/mol.K) is the universal gas constant.

D–R model is also represented in Eq. 13 as:

$$\ln q_e = \ln q_o - K_{ad}\varepsilon^2 \tag{13}$$

where q_{ad} is a constant related to adsorption mean free energy and q_s is the D–R adsorption capacity at monolayer saturation, while ε is called Polanyi potential.

Adsorption thermodynamics

The thermodynamics studies of Mn, Fe, Pb and Cu ions adsorption onto AAC and AAC-TiO$_2$ were carried out at temperatures; 30, 40, 50, 60 and 70 °C, respectively. This was carried out to know the influence of temperature on the removal efficiency of the metal ions from wastewater. Change in enthalpy (ΔH°), change in Gibbs free energy (ΔG°) and entropy change (ΔS) of the system during the adsorption process were evaluated with Eq. (14)–(17)

$$\Delta G_{ads} = \Delta G° + RT \ln Q \tag{14}$$

The change in Gibbs free energy (ΔG, kJ/mol) of the metal ion(s) adsorption progression was determined by Eq. (13) where Q designates the quotient of reaction, and relate to the metal ion concentrations of a system that is not in equilibrium. But, at equilibrium $\Delta G_{ads} = 0$ making Eq. (14) reduced to Eq. (15)

$$\Delta G° = -RT \ln Kd \tag{15}$$

where

$$Kd = \frac{q_e}{C_e} \tag{16}$$

$$\ln K_d = -\frac{\Delta G^0}{RT} = \frac{\Delta S}{R} - \frac{\Delta H^0}{RT} \tag{17}$$

where K_d is the equilibrium parameter signified by Eq. (16), q_e and C_e are the quantity of metal ion adsorbed and the concentration of each metal ion in the solution at equilibrium.

The ΔH° and ΔS° values were obtained from the slope and intercept of the Van't Hoff plots of In K_d against $1/T$ given in Eq. 17 (Bankole et al. 2019).

Analysis of error

To remove or minimise error in the data obtained from the figures of each experiment, analysis were duplicated and subjected to statistical analysis. The constants from the isotherm and kinetics studies were determined using Origin pro (2019a) software at a very high accuracy level. The linear determination coefficient (R^2), the non-linear Chi-square test (X^2) and the sum of square error (SSE) tests were performed to further choose the best-fitted isotherm and kinetic models. The mathematical equations are given in Eqs. 18 and 19:

$$X^2 = \sum \left(\left(q_{e,\exp} - q_{e,\text{cal}} \right)^2 \middle/ q_{e,\text{cal}} \right) \tag{18}$$

$$\text{SSE} = \sum \left(q_{e,\exp} - q_{e,\text{cal}} \right)^2 \tag{19}$$

Results and discussion

Phytochemical analysis of plant leaves

The collected plant leaves of *Parkia biglobossa* L. were assessed for their phytochemical constituents using the standard analytical methods and the result is presented in Table 1. It was observed that the *Parkia biglobossa* L. leaves have a considerable amount of phytochemical contents of Phenols, Flavonoids and Tannins. Studies have shown that these three phytochemicals contents are responsible for the stabilization and capping of metal oxide nanoparticles. The result is indicative of the fact that *Parkia biglobossa* leaves can be used for the synthesis of the nanoparticles. The confirmed phytochemicals present are in agreement with the findings of Dedehou et al. (2016) and Yusof et al. (2018).

Table 1 Phytochemical analysis of *P. biglobossa* leaves

Phytochemicals	Interference
Tannin	+
Flavonoids	+
Phenol	+
Steroids	+
Phlobatannins	−

Key (+) present (−) absent

UV–visible spectroscopic analysis of TiO$_2$ nanoparticles

During the synthesis of titanium oxide nanoparticles, colour changes from greenish-brown of the leaf extract to a light brown solution were observed. This effect is called Tyndall effect which indicates the formation of nanoparticles in the solution (Soni et al. 2018). UV–visible spectrophotometer spectra of the synthesized titanium (IV) oxide nanoparticles is shown in Fig. 1. The figure revealed the presence of an absorption band at 358 nm. The band obtained is relatively close to 350 nm reported in the literature (Swathi et al. 2019), where TiO$_2$ nanoparticles were synthesised with *Cassia fistula* leaves. The difference between the wavelength peaks might be due to the difference in precursor salt and the type of leaf extract (*P. biglobossa*) used for the preparation of TiO$_2$ nanoparticles.

FTIR analysis of AAC and TiO$_2$-AAC

The Fourier Transform Infrared spectroscopic analysis of the AAC and TiO$_2$-AAC are presented in Fig. 2a and b. Several medium or low intense absorption bands can be noticed on the spectral of the AAC at 3857.76 cm^{-1} and 3734.31 cm^{-1}. The absorption bands were assigned to the O–H group stretch (Fig. 2a). The absorption bands at 3618.58 cm^{-1} represent OH bridging hydroxyls in the kaolin cages, bonded as Al–OH–Si similar to those observed in zeolite cages (Guillaume et al. 2018). The peaks between 3417.98 cm^{-1} and 3217.37 cm^{-1} suggest the O–H–O stretch of water molecules (Krishnan and Mahalingam 2017). The peak at 2337.80 cm^{-1} may be attributed to adsorbed CO$_2$ while the peak 1681 cm^{-1} is related to–OH bend in water molecules found in typical kaolin clays (Kenne-Diffo et al. 2015). Similar peaks were also on the TiO$_2$–AAC, however with a slight shift and reduced intensity especially for the bonded hydroxyl group on TiO$_2$-AAC. The reduction in the intensity may be ascribed to the incorporation of Ti onto the kaolinite clay lattice. Also, the additional peaks at 914.87 cm^{-1}, 869.92 cm^{-1}, and 438 cm^{-1} were ascribed to the formation of Ti–O–Ti bonded, evidence of titanium (IV) oxide doping on the lattice layer of AAC, and by extension indicative of TiO$_2$ pillared within the clay matrix (Guillaume et al., 2018).

Fig. 1 UV–visible spectroscopy of synthesised TiO$_2$ using extract of *Parkia biglobossa* leaves
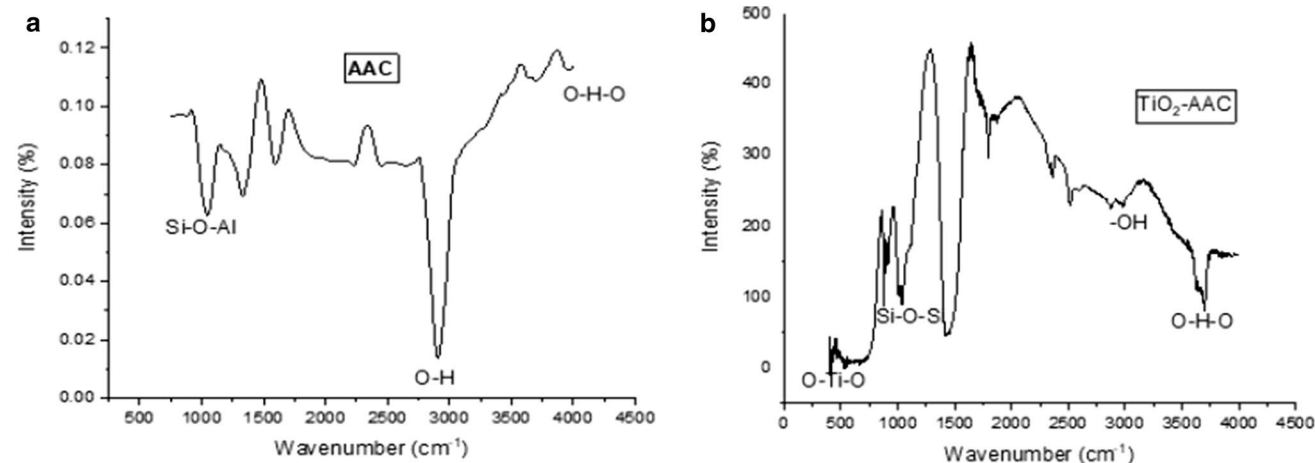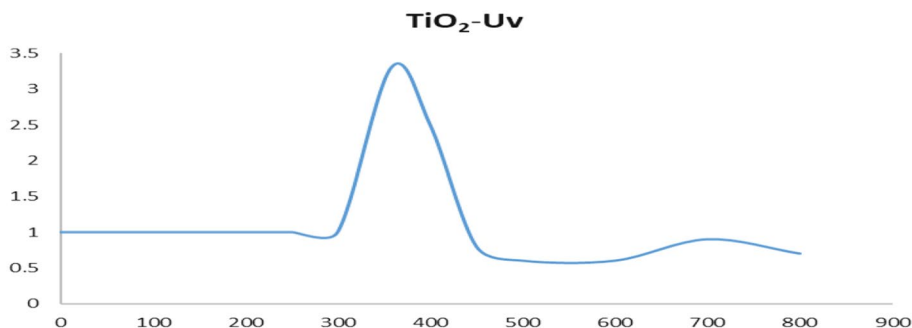

Fig. 2 FTIR spectral of **a** AAC and **b** TiO$_2$–AAC

XRD result

X-ray diffraction (XRD) analysis was employed to show the crystallographic and mineralogical representation of the prepared samples. Figure 3a–c represents the XRD pattern of the acid-activated clay (AAC), TiO_2 and TiO_2 modified acid-activated kaolinite clay (TiO_2-AAC). As shown in Fig. 3a different diffraction peaks were observed at 2 theta value of 12.36°, 19.92°, 24.80°, 26.39° 35.91°, 37.71°, 38.4° and 62.34° with miller indices; (001), (020), (002), (003), (-131), (003), (-113) and (060), respectively. This corresponds to the presence of kaolinites type of clay. Other diffraction peaks on the AAC spectral at 2Θ values of 20.93° (100), 26.59° (101), 36.48° (110), 50.00° (112) and 68.57 (134) (JCPDS card no-083–0539), indicating the presence of quartz in the acid-activated kaolinite clay with average crystallite size of 8.10 nm. On the other hand, the XRD pattern of TiO_2 revealed spectral the presence of strong, sharp and moderately intense diffraction peaks at 2Θ values of 27.45°, 36.16°, 39.20°, 44.05°, 54.32, 56.64° and 69.79°. These peaks allied well to the crystal planes of (110), (111), (200), (210), (211), (220) and (112) with

(JCPDS number 00-021-1276) for a typical rutile phase of TiO_2 with calculated crystallite size of 9.48 nm. The crystallite size of TiO_2 obtained in this study, is smaller and preferred than the earlier reports by Patidar and Jain (2017) who obtained 12.22 nm crystallite size for anatase titanium-dioxide prepared using *Moringa oleifera* leaves extract as a reducing agent. Zahir et al. (2015) obtained a 12.82 nm crystallite size anatase phase of TiO_2 using *Euphorbia prostrata,* Landage et al. (2020) also obtained a 20 nm-sized anatase-phase TiO_2 using *Staphylococcus aureus*. Subhapriya and Gomathipriya (2018) obtained a 30 and 25 nm crystallite size TiO_2 using *Trigonella foenum* with anatase cum rutile phase titanium synthesised while 92 nm crystallite sized anatase TiO_2 nanoparticles were obtained by Abu-Dalo et al. (2019) using pristine pomegranate peel extract. Most of the synthesised TiO_2 reported are anatase or mixed phases but not pure rutile-phased TiO_2, the difference in phase and size of TiO_2 nanoparticles obtained were attributed to the nature of plant extracts and calcination temperature used during the synthesis. XRD spectra of TiO_2-AAC revealed the existence of sharp and intense diffraction peaks of at 2
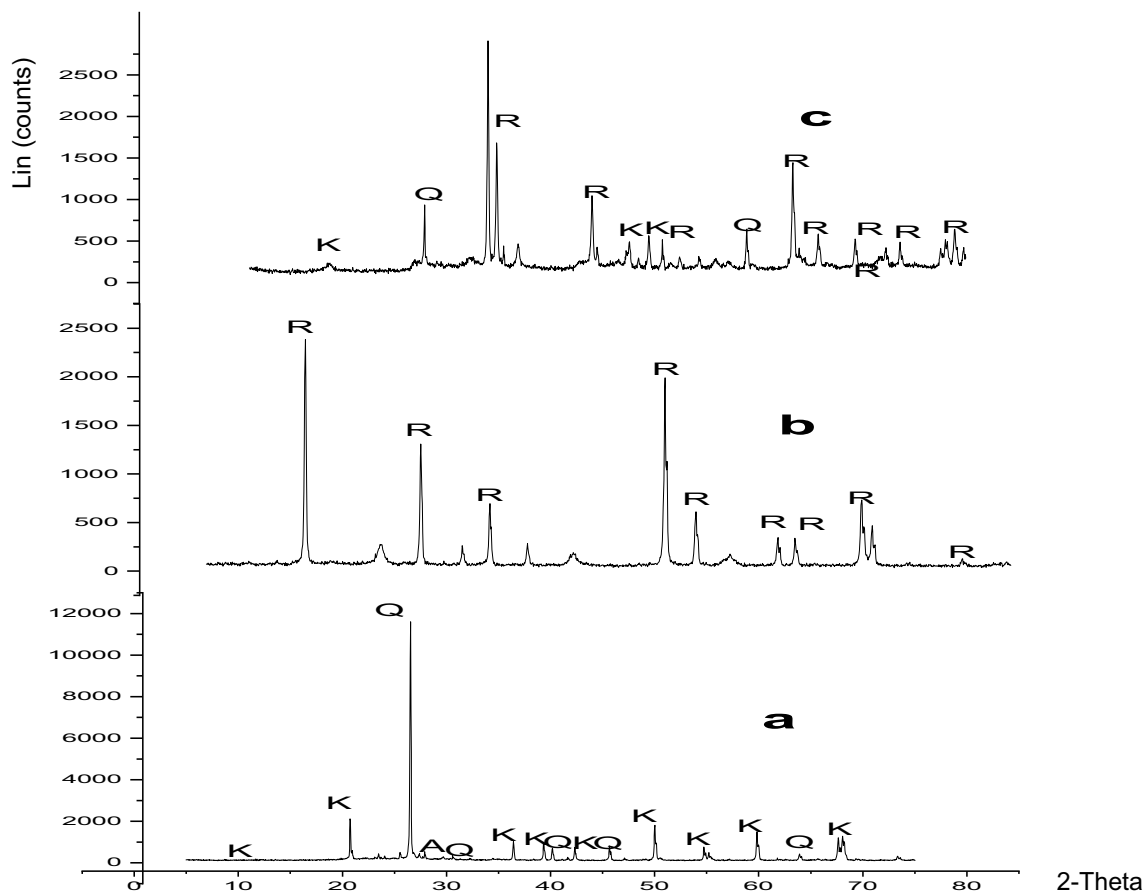

Fig. 3 XRD patterns of synthesised **a** AAC, **b** TiO_2 and **c** TiO_2–AAC

theta value with corresponding miller indices of 12.43° (001), 26.59 (101), 34.90° (-130), 36.10° (110), 39.43° (012) and 40.42° (111) 27.52° (110), 41.22° (111), 44.05° (210), 54.32° (211), 56.70° (220). The characteristic peak of acid activated clay signified at 26.59° (101) was overlap (110) plane of TiO_2. A similar observation was noticed with for peak at 54.71° (202), with overlapping effect on (211) plane of rutile TiO_2. The overlapping phenomenon is evidence of the doping effect of kaolinite clay on TiO_2 structure. The intensity of other diffraction peaks at 41.22° (111), 44.05° (210), 54.32° (211), 56.70° (220), 62.90° (002), 64.03° (310), and 69.28° (301) reduced due to the incorporation of kaolinite clay on TiO2 matrix. The reduction of crystallite size TiO_2-AAC (6.11 nm) compared to TiO_2 alone is evidence of improved dispersion of the TiO_2 on the AAC framework.

HRSEM/EDS of the nanoparticles and composite

The HRSEM of acid-activated kaolinite clay (AAC) and titanium (IV) oxide–activated clay (AAC-TiO_2) are presented in Fig. 4a, and b. Figure a shows a well ordered, well-defined arrangement of kaolinite plates with induced porosity and smooth surfaces, due to acid treatment. Figure 4b shows the arrangement of well ordered, well-defined intercalated, grain-like porous surface. The immobilization of the TiO_2 onto acid-treated kaolinite clay showed a well dispersed and homogeneous distribution of spherical particles, and evidence the titanium (IV) oxide doped on the acid-activated clay surface.

The EDS result in (Fig. 5a and b) reveals the characteristic lines of carbon, oxygen, aluminium and silicon as the major elements in the acid-activated kaolinite clay and the
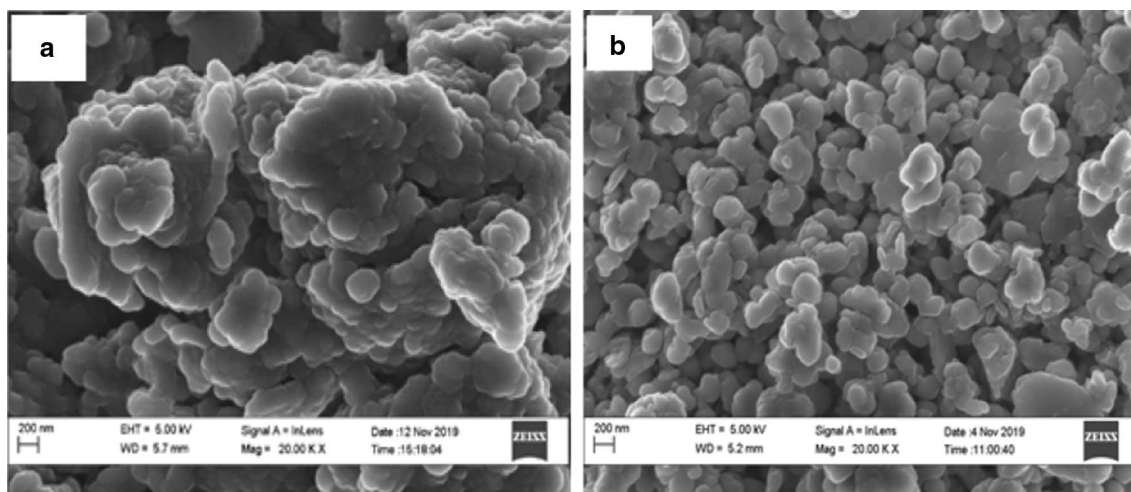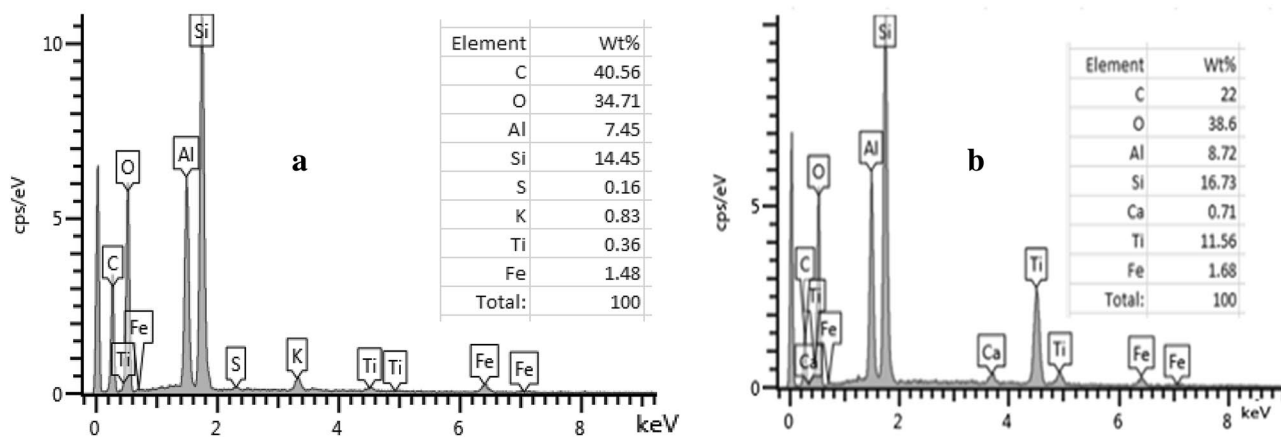

Fig. 4 HRSEM of **a** AAC **b** TiO$_2$–AAC

Fig. 5 EDS spectrum of **a** AAC **b** TiO$_2$–AAC

TiO_2 doped activated kaolinite clay. Calcium, titanium, sulphur and iron were also detected on the acid-activated clay. The sulphur was probably from the residual tetraoxosulphate (IV) acid used for acid activation. The percentages of the identified elements increased in Fig. 5b, due to the interaction of TiO_2 with the acid-activated clay. The reduction in oxygen wt.% in the TiO_2–AAC as compared with that in TiO_2 is attributed to bonding with the Si and Al in the acid activation clay.

BET analysis of AAC, TiO_2 and TiO_2-AAC composite

The N_2 adsorption-desorption curve for the three materials (AAC, TiO_2 and TiO_2-AAC) is shown in Fig. 6, while the parameters (surface area, pore diameter and pore volume) are presented in Table 2. The TiO_2 has 10.23 m²/g of surface area while the AAC has 14.15 m²/g which shows that the latter has a larger surface area than the former. This claim is similar to the findings of Akinnawo (2019); Krishnan and Mahalingam (2017) where they also reported low surface area for TiO_2. However, the higher surface area of the TiO_2–AAC (32.98 m²/g) was due to modification by the rutile-TiO_2 which agrees with the literature (Bok-Badura et al. 2018; Krishnan and Mahalingam 2017). The specific surface area and pore volume of TiO_2–AAC were significantly increased to 32.98 m²/g due to the dispersed stacking of TiO_2 on the surface of the acid-activated clay.

However, the pore diameter of the prepared TiO_2–AAC decreased after the modification by TiO_2 due to the in-situ

Table 2 BET surface area, pore diameter, pore volume of AAC, TiO_2 and TiO_2–AAC

Sample	Surface area m²/g	Pore diameter (nm)	Pore volume (cc/g)
AAC	14.15	17.66	0.069
TiO_2	10.23	4.09	0.093
TiO_2-AAC	32.98	4.86	0.150

deposition of the TiO_2 on AAC, which blocked a large number of accumulated pores on TiO_2–AAC. On the other hand, the TiO_2–AAC composite has a large specific surface area and pore volume, which is conducive for the removal and capturing of pollutants molecules from the aqueous matrix by the composite materials. According to the IUPAC classification, the three samples demonstrated a typical type IV adsorption isotherm of a typical mesoporous structure, similar to the one obtained by Malima et al. (2018). Besides, pure TiO_2 has a typical H1 hysteresis loop, which indicated the stacked mesoporous structure derived from the accumulated spherical particles. Other samples display H3 hysteresis loops, which indicates that they have irregular mesopores and macropores due to the irregular shape of particles and the composition of different components. The construction of a combined structure improves the particular surface area and pore volume of the TiO_2–AAC. The extensively constructed mesopores give the TiO_2–AAC significant adsorption capacity, which may enhance the adsorption ability of

Fig. 6 BET adsorption–desorption isotherms plots of **a** AAC, **b** TiO_2 and **c** TiO_2–AAC
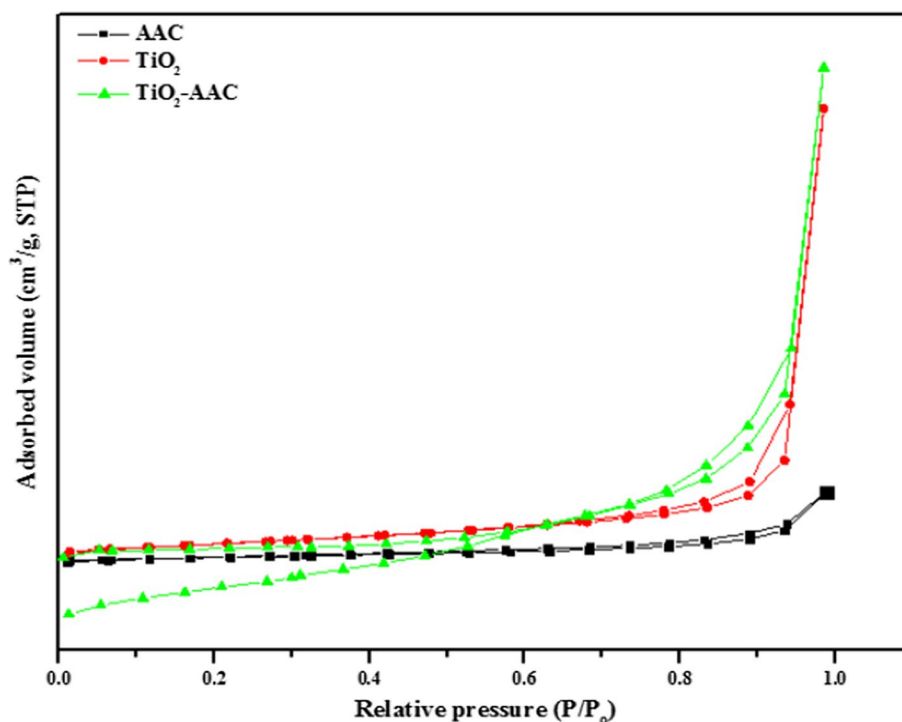
the TiO_2–AAC materials than the other two materials (Xiang et al. 2019).

XPS analysis of AAC and TiO$_2$–AAC

The XPS analysis was conducted to determine the surface oxidation state and orbital of each element present in the samples. Figures 7ai and ii shows the general survey spectrum of the rutile titanium dioxide nanoparticles, activated clay (AAC) and titanium (IV) oxide–activated clay The XPS of the activated clay sample (Fig. 7ai), reveals the presence of Si ($2p$) at binding energies of 103.14(eV), C (1 s) at 284.8 eV. A narrow but sharp peak of oxygen (1 s) occurs at the binding energy of 529.7 eV. The Si Originated from the acid-activated clay because clays are generally made up of aluminium and silicon (alumino-silicates) elements but in varied ratios (Pimneva 2019). Figure 7aii (TiO_2–AAC XPS spectral) revealed the presence of Ti ($2p_{3/2}$) orbital at a binding energy of 458.3 eV, while a sharp narrow peak of oxygen (1 s) was also found at the binding energy of 529.7 eV and carbon (1 s) at 284.8 eV. The narrow and sharp peak seen around binding energies of 458.34 eV shows the presence of Ti $2p_{3/2}$. This confirms the formation of pure rutile TiO_2. The binding energies obtained for titanium and oxygen matched well with the literature (Krishnan and Mahalingam 2017).

Figure 7b displays the XPS of Ti $2p$ deconvoluted spectra in TiO_2 and TiO_2–AAC. The figure reveals the presence of two sharp peaks on each deconvoluted spectra at

Fig. 7 XPS spectral of **a i** AAC, **ii** TiO$_2$–AAC and **b** deconvoluted spectral of Ti in TiO$_2$ and TiO$_2$–AAC
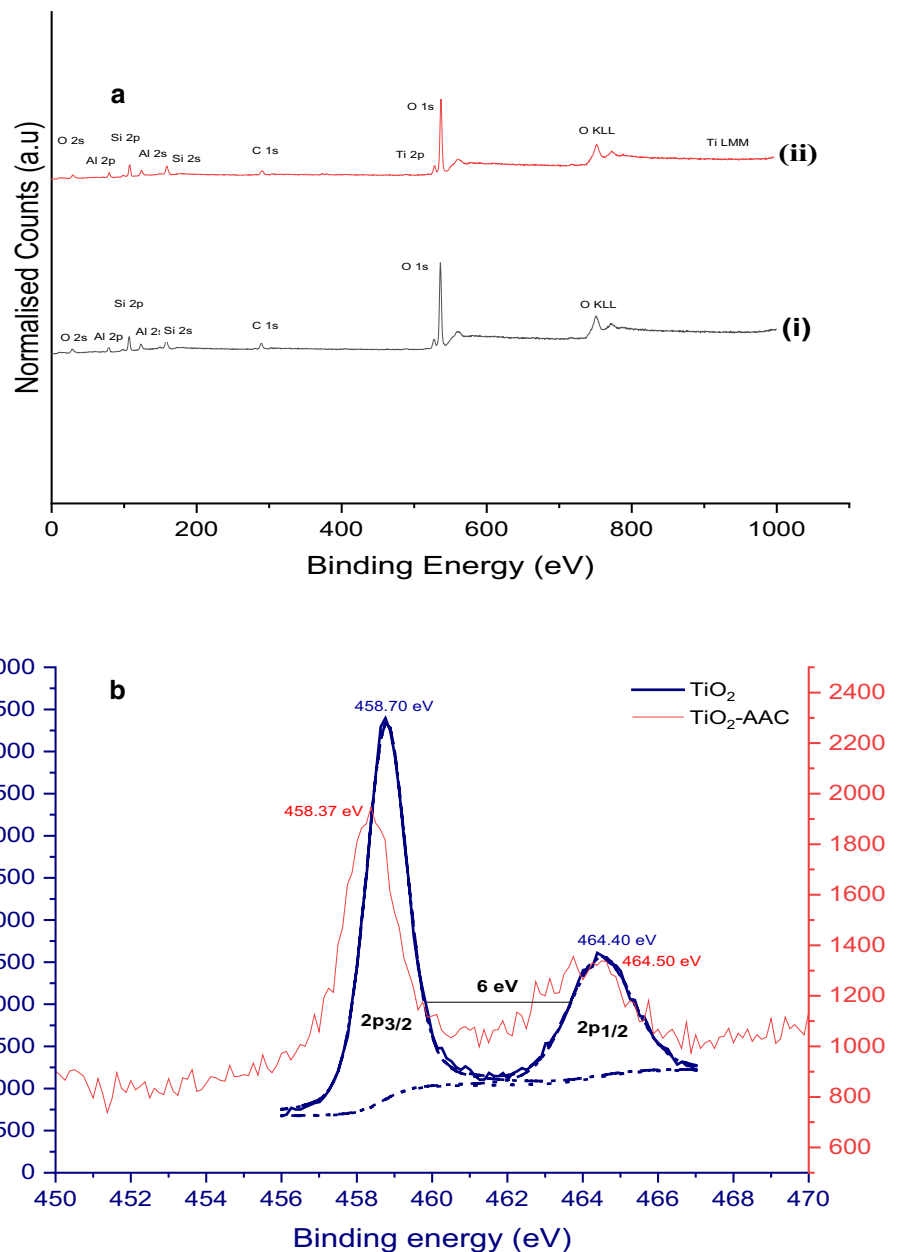
binding energies of 458.70 eV and 464.40 eV in TiO_2, with 458.37 eV and 464.50 eV in TiO_2–AAC respectively, for the XPS deconvoluted spectrum in the Ti 2p region. These peaks are assigned to $2p_{3/2}$ and $2p_{1/2}$, both spectral shows the difference of 5.80 and 6.03 eV (~ 6 eV), an indication that the TiO_2 exists in the oxidation state of + 4 in the spectra of both TiO_2 nanoparticles and TiO_2-AAC despite the modification. This corroborates the reported values in the literature (Li et al. 2015).

Heavy metals characterisation of the mining wastewater.

The mining site wastewater was characterised for the presence of heavy metals concentrations present therein. The table, therefore, presents the heavy metals, concentrations in the mining wastewater and their standard organisation permissible limit (Table 3).

From the table, it was observed that the mining wastewater has a pH higher than the permissible in drinking water by both WHO and NIS standards. The pH is a serious but simple parameter that determines most chemical reactions in aquatic mediums. Very high or very low pH value can be harmful to aquatic life. The pH of the mining waste water is acidic due to the acid mine drainage generation process. This acidic water can cause different skin diseases and the death of aquatic organisms due to sensitivity (Masindi and Muedi 2018). Moreover, the presence of heavy metals such as Fe, Cu, Mn, Ni, Cd, Pb and Cr in wastewater have been reported to cause; mental retardation (Pb), skin rashes, respiratory problems(Cr), critical renal failure (Mn), debilitated immune systems, liver and kidney damage, cancer, chest pain, rapid respiration (Ni) (Balali-Mood et al. 2021; Lakherwal 2014). It can be seen from the Table that iron has a concentration of 20.013 mg/L, which is greater than the WHO standard of 3 mg/L but lesser than 64.96 mg/L obtained by Kamal and Gooyong (2019) from an AMD, nickel was 0.326 mg/L below WHO permissible

Table 3 Heavy metals parameters in the mining wastewater

Parameter	Initial values	WHO/EPA (2017)	NIS (2015)
pH	5.92	6.50–8.50	6.50–8.50
Fe (mg/L)	20.02	1.00–3.00	0.3
Cu (mg/L)	0.31	0.05	1
Mn (mg/L)	4.29	0.05	0.2
Cd (mg/L)	ND	0.005	0.003
Ni (mg/L)	0.33	3.00	0.02
Pb (mg/L)	0.98	0.015	0.01
Cr (mg/L)	0.10	0.10	0.05
Colour	Dark	Clear	Clear
Odour	Offensive	Odourless	Odourless

limit concentrations of 3.0, therefore acceptable. Low Ni concentrations of 1 and 2.97 mg/L was also obtained by Esmaeili et al. (2019) and Masindi and Muedi (2018). Previous studies documented varied concentrations of pollutants in mining wastewater (Kamal and Gooyong 2019; Madzivire et al. 2011; Masindi and Muedi 2018). Xie et al. (2018) reported 0.008–3.355 mg/L of Cu, 0.058–0.349 mg/L of Pb, 0.035–0.476 mg/L of Ni, and 0.006–0.022 mg/L of Cr all lower than the values obtained in this study (Chanchaga mining wastewater). Variations observed in heavy metal ion concentrations at various sites is due to; the pH variation of the concerned AMD. This is because concentrations decrease when pH increases (Masindi and Muedi 2018). Additionally, the presence of dark colour (coloured water) and foul odour as presented on the Table in the mining wastewater is a characteristic property of AMD (Kefeni et al. 2017; Seo et al. 2016). This earlier listed contaminants at their concentrations make life difficult for aquatic species due to low oxygen content. The earlier mentioned contaminants level revealed that the mining wastewater cannot be directly released into the environment without proper treatment and therefore, the need for adsorptive removal of the heavy metals using AAC and TiO_2–AAC.

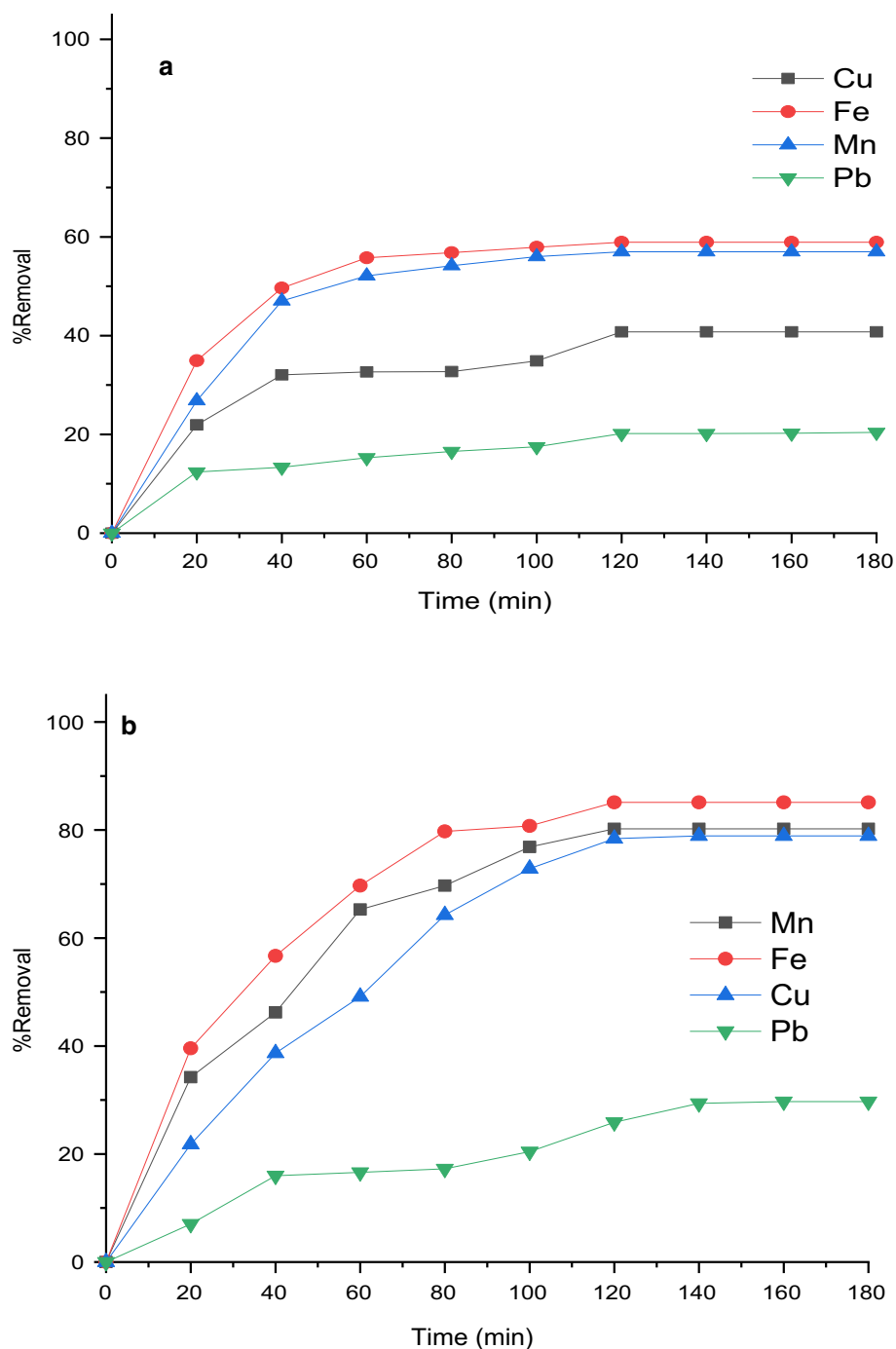## Metal ion adsorption experimental results

Effect of contact time

Figure 8a and b depicts the effect of variation of contact time on the uptake of Mn (II), Fe (III), Pb (II) and Cu (II) from mining wastewater onto the AAC and TiO_2–AAC. The quantity of each metal ion adsorbed was found to increase with increased time from 20 to 180 min for the two adsorbents. AAC steadily removed 57.00% Mn (II), 40.76% Cu (II), 58.92% Fe (III), and 20.17% Pb (II) maximum at an equilibrium time of 140 min. There was a drastic increase in the percentage removal by the TiO_2-AAC at the first 60 min compared to AAC alone and continued gradually until 120 min, with total removals of 80.23% Mn (II), 85.12% Fe (III), 78.42% Cu(II) and 20.42% Pb (II) (Fig. 8b). Rapid initial adsorption may be attributed to available surface adsorption sites on AAC and TiO_2–AAC. Adsorption equilibrium on the surface of TiO_2–AAC was completely attained at 120 min for Mn (II), Pb (II) and Cu (II) ions, while Fe (III) ions had reached equilibrium with total removal at the first 80 min of the adsorption experiment. The difference in equilibrium time of adsorption of each ion may be attributed to ionic radii, selectivity of the heavy metal by the adsorbents, the surface charge of adsorbent and difference in hydration energy; Cu (− 2010 kJ/mol), Mn (− 1760 kJ/mol) and Pb ions (− 1481 kJ/mol). The higher the hydration energy, the faster the ease of adsorption (Zendelska et al. 2018). The order of removal

Fig. 8 Effect of time on the adsorption of metal ions by **a** AAC **b** TiO$_2$–AAC using 0.5 g adsorbent dosage, 30 °C temperature and 20–180 min contact time


being; Fe (III) > Mn (II) > Cu (II) > Pb (II) As time progresses from 80 to 120 min, the adsorptive surfaces on the TiO$_2$–AAC were saturated with metal ions resulting in the repulsion between the adsorbed ions on the adsorbent material and those in the bulk solution signifying attainment of equilibrium for the four ions. The enhanced adsorptive performance of TiO$_2$–AAC more than AAC alone can be linked to higher surface area and more functional groups of the former adsorbent than the latter one.

Effect of adsorbent dosage

The effect of adsorbent dosage on Mn (II), Fe (III), Pb (II) and Cu (II) ions adsorption from mining wastewater onto AAC and TiO$_2$–AAC was investigated and the results are presented in Fig. 9a and b. As shown in Fig. 10a, it was noticed that the uptake level of Mn (II), Fe (III) and Pb (II) ions increase as the dosage increased from 0.1 to 0.4 g, with 69.80% for Mn (II), 59.57% for Fe (III), 68.47% for Pb (II),

Fig. 9 Effect of **a** AAC and **b** TiO$_2$–AAC adsorbent dosage on the adsorption of metal ions using 0.1–1.0 g adsorbent dosage, 70 °C temperature and 120 min contact time
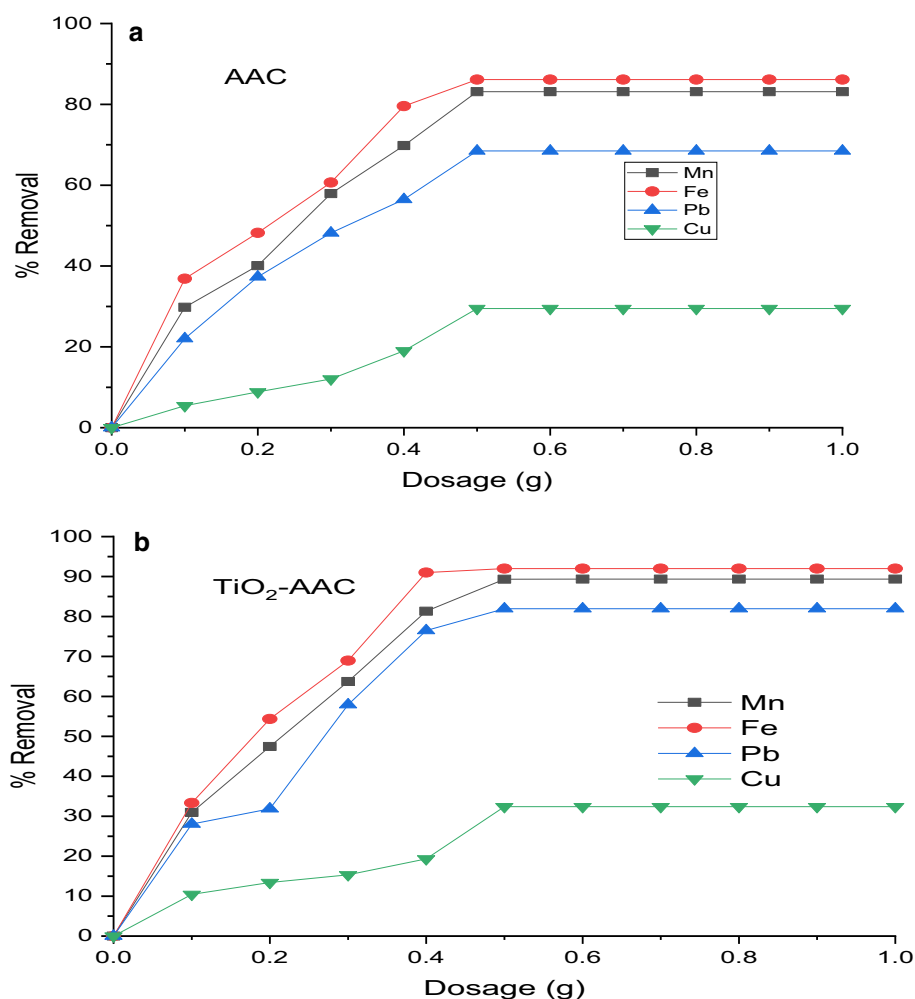

while 19.00% of Cu (II) was removed. When 0.5 g dosage was used, 83.12%, 86.13% and 68.47% of Mn (II), Fe (III) and Cu (II) ions were removed respectively, (see Fig. 9a), however, the percentage removal of Pb (II) ions was only 29.48% using 0.5 g adsorbent dosage. No substantial change is observed in the percentage removal of the four ions when the dosage was increased from 0.6 to 1.0 g. This observation can be explained in terms of exposure to substantial number of accessible binding sites to the small adsorbate in the medium, which resulted to less per gram adsorption. This prevented the nanoadsorbent with dosage greater than 0.5 g to be shielded from further adsorbing heavy metal ions (Adebayo et al. 2020).

The removal efficiency of the four ions with AAC and TiO$_2$–AAC increasing dosage of 0.1–1.0 g increase relatively. This is as result of an increase in the number of active sites available for the adsorption process (Abunah et al. 2019). However, there is no desirable change in the adsorptive capacity of Pb (II) ions even at maximum adsorbent dosage, as Pb (II) was the least adsorbed (29.48%). Mn (II), Fe (III) and Cu (II) ions, % removal

onto AAC were 83.12, 86.13, 68.47%, respectively, while AAC-TiO$_2$ had percentage removal up to 89.34%, 91.97%, 76.47% and 32.39% respectively for Mn (II), Fe (III), Cu (II) and Pb (II). It was observed that at every dosage of the adsorbent, TiO$_2$-AAC sequestered more of the heavy metals ions than AAC due to its higher surface area and more functional groups than AAC alone. From the results, it was observed that there was strong selectivity among the metal ions by the active sites based on their ionic radius. It was found that the ions with smaller ionic radius diffused faster (onto the adsorbent surface) than the heavier ones. This is in the migration order of; Fe (III), 0.06 nm > Mn (II) 0.072 nm > Cu (II) 0.073 nm except for Pb (II) ions 0.119 nm which is heavy and has high ionic radii, thus retarding its diffusion capability onto the pores of the adsorbent. The result is similar to the report of Mobasherpour et al. (2012), who considered comparative adsorption of Pb (II), Cd (II) and Ni (II) from aqueous solution onto nano crystallite hydroxyapatite and found that ionic radii of the competing metal ions affect the rate of their adsorption from the aqueous solution.

Fig. 10 Effect of temperature on the adsorption of metal ions onto **a** AAC and **b** TiO$_2$–AAC using 0.5 g adsorbent dosage, 30–70 °C temperature and 120 min contact time
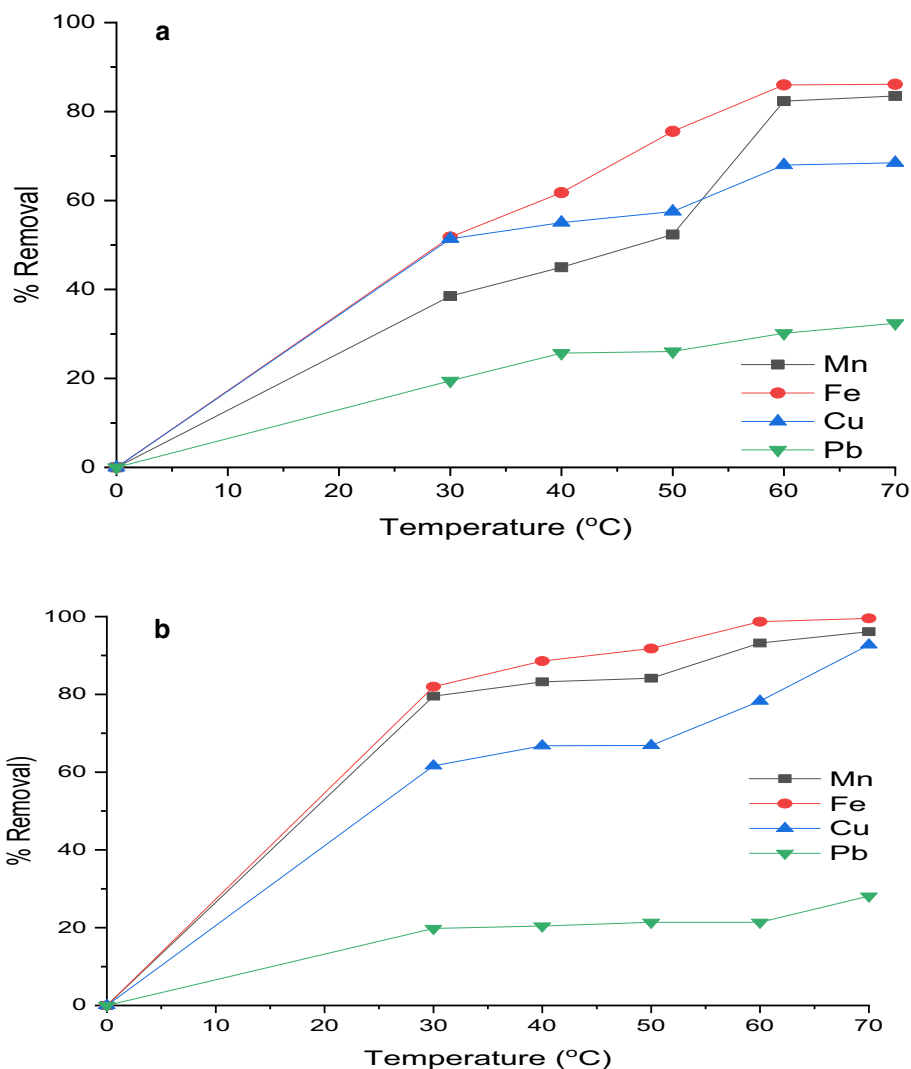
Effect of temperature

The percentage removal of Mn (II), Fe (III), Pb (II) and Cu (II) ions by the AAC and AAC–TiO$_2$ was studied as a function of temperature from 30, 40, 50, 60 and 70 °C and the result presented in Fig. 10a and b. The effect of temperature is an important parameter to be studied in adsorption processes because, the type of reaction and the reaction mechanism of the adsorption process can be evaluated (Alaya-Ibrahim et al. 2019). Adsorption can be physical or chemical depending on the type of attraction binding the adsorbate onto the adsorbent. From the figures, the percentage removal of Mn (II), Fe (III), Pb (II) and Cu (II) ions by the AAC and TiO$_2$–AAC improved sharply, as the temperature increases from 30 to 50 °C. As the temperature increases to 60 and 70 °C, a comparable amount of metal ion was removed by the two nano adsorbents. For the AAC, the maximum removal efficiency of 83.45,

86.13, 68.47 and 29.39% were obtained for Mn (II), Fe (III), Cu (II) and Pb (II) ions respectively at 70°C. On the TiO$_2$–AAC, it was discovered that, the percentage removal of Mn (II), Fe (III), Cu (II) and Pb (II) ions also increased steadily with an increase in temperature from 30 to 70 °C with 89.36% Mn (II), 91.99% Fe (III), 81.94% Cu (II) and 32.39% Pb (II) ion removal at maximum. The increase in efficiency of the nanocomposite material accompanied by increase in temperature from 30 to 70 °C may be due to the increased mobility (Alaya-Ibrahim et al. 2019) of the heavy metals towards the binding sites on TiO$_2$–AAC than AAC as temperature increases. It was also noticed that the adsorbent performance under the influence of temperature was in the order of TiO$_2$–AAC > AAC. Therefore, the adsorption taking place may be described as a chemisorption process (Alaya-Ibrahim et al. 2019; Bankole et al. 2019).

Adsorption Isotherms of the AAC and TiO₂-AAC

The interaction of the raw mining wastewater containing 4.291 mg/L Mn(II), 20.013 mg/L Fe (III), 0.975 mg/L Cu (II) and 0.313 mg/L Pb (II) ions with the AAC and TiO$_2$–AAC shows a reduction in the metal ion concentration at equilibrium to 0.155 mg/L Mn(II), 0.014 mg/L Fe (III), 0.01 mg/L Cu(II) and 0.128 mg/L Pb (II) respectively. The values obtained using both adsorbents were lesser than their permissible standard concentration in drinking water as stated by EPA and WHO (WHO 2017). The equilibrium data were evaluated using Langmuir, Freundlich, Temkin and D–R isotherm models. The interaction was carried out to correlate the equilibrium experimental data of Mn (II), Fe(II), Pb(II) and Cu (II) adsorption by the AAC and TiO$_2$–AAC (see Table 4). The isotherms were compared using the correlation coefficient R^2, SSE and X^2. Of all the fitted isotherms (Langmuir, Freundlich, Temkin and D-R models), the Langmuir isotherm best described the adsorption process by the two adsorbents, depicting a homogenous and monolayer coverage by the AAC and TiO$_2$–AAC. The R^2 values were between 0.997 and unity for AAC, between

0.999 and unity also for TiO$_2$–AAC. The monolayer adsorption capacities between 0.192 and 3.957 mg/g were obtained for AAC while between 2.00 and 3.988 mg/g respectively. The improvement in the values obtained from TiO$_2$-AAC could be attributed to the modification on the surface by TiO$_2$ which improved the surface area based on the synergistic effect of the combined adsorbents (Abunah et al. 2019). The value of the dimensionless equilibrium parameter (R_L) calculated as shown in Table 4, for Mn(II), Fe(II) and Cu(II) ions shows that the adsorption process was favourable ($0 < R_L < 1$) (Miyah et al. 2017) except for Pb (II) ion on TiO$_2$–AAC, whose value of 1.9, depicting that, Pb ion adsorption onto AAC–TiO$_2$ was not so favourable. The lowest values obtained from the error analysis of the Langmuir model, by the statistical parameters (X^2 and SSE) also validated the fitness of the Langmuir model when compared with the Freundlich, Temkin and D-R model. According to Langmuir isotherm, this means that: (i) it was not possible for adsorption of three the metal to advance outside monolayer coverage. (ii) the active sites on the surface of AAC and TiO$_2$-AAC were equivalent and only take a molecule of the adsorbate. (iii) the ability of heavy metal molecules to

Table 4 Isotherm parameters for heavy metals removal from mining wastewater onto AAC and AAC–TiO$_2$

	AAC				TiO$_2$–AAC			
	Mn(II)	Fe(III)	Cu(II)	Pb(II)	Mn(II)	Fe(III)	Cu(II)	Pb(II)
Langmuir								
q_m (mg/g)	0.783	3.957	0.149	0.019	0.678	3.989	0.169	0.002
K_L (L/min)	120.491	4211.67	278.846	16.525	25.618	83,566.7	280.009	4.805
R_L	$1.94E-03$	$1.19E-05$	$3.69 E-03$	0.240	$9.18E-03$	$5.98E-07$	$3.67 E-03$	1.984
R^2	1	1	0.9968	0.999	0.9993	1	0.9994	0.7925
SSE	$1.95E0-3$	$1.74E-03$	$2.08E-03$	$3.04E04$	$1.92E-02$	$2.00E-04$	$3.89E-04$	$3.02E-04$
X^2	$2.50E-03$	$4.40E-04$	$1.39E-02$	$1.55E-02$	$2.83E-02$	$5.03E-05$	$2.30E-03$	$1.86E-01$
Freudlich								
N	21.645	312	7.337	1.2274	9.259	312.5	16.077	0.222
K_f (mg/g)	0.759	3.948	0.123	0.007	0.152	$2.205E-05$	1	1
R^2	0.998	0.858	0.970	0.999	0.9818	0.993	0.963	0.923
SSE	1.216	6.894	5.240	24.469	1.4011	6.907	2.862	11.537
X^2	4.412	5.020	2.502	4.984	3.813	5.024	1.522	10.760
Temkin								
b_T (kJ/mol)	$-30,387.7$	$-195,282$	$-110,489$	$-91,605.2$	$-30,387.7$	$-195,282$	$-222,933$	$-50,585.18$
A_T (L/g)	$2.13E-09$	$9.52E-13$	$5.90E-03$	2.032	$2.42E-04$	$7.65E-13$	$1.73E-06$	$3.21E-01$
R^2	0.999	0.858	0.975	0.999	0.895	0.993	0.967	0.998
SSE	0.007	2.874×10^{-4}	0.0013	9.030×10^{-7}	0.007	2.874×10^{-4}	0.0013	9.030×10^{-7}
X^2	9.49×10^{-4}	7.185×10^{-5}	2.604×10^{-4}	1.300×10^{-7}	9.49×10^{-4}	7.185×10^{-5}	2.604×10^{-4}	1.300×10^{-7}
D–R								
K_{ad}	0.2495	1.358	1.973	4.295	0.3691	1.3788	1.7333	8.9582
R^2	0.996	0.543	0.9299	0.9978	0.9419	0.9864	0.9341	0.9072
E	1.416	0.607	0.503	0.341	1.164	0.602	0.537	0.236
SSE	0.029	5.64×10^{-5}	0.190	0.210	0.032	3.24×10^{-5}	0.169	0.212
X^2	0.004	1.14×10^{-5}	0.027	0.029	0.005	1.159×10^{-5}	0.038	0.031

adsorb at a specified site is not dependent on the accommodation of the neighbouring site (Ait Ahsaaine et al. 2018).

As shown in Table 4, it can be observed that TiO$_2$-AAC was determine to be more efficient for the sorption of heavy metals from the raw mining wastewater with a removal percentage (91.99%) higher than that of Guillaume et al. (2018) who used titanium oxide clay to adsorb 27.05% Cd ion. Most of the adsorption process kinetics agrees with the PSO kinetics model and Langmuir isotherm except for Mustapha et al. (2019) whose kinetics and isotherm followed Avrami, Jovanovic and Redlich-Peterson models, respectively. Other studies with higher values of adsorptive capacity than the presented in Table 4, used simulated wastewater, which did

not involve (multiple competition among the heavy metal ions). Similarly, Martinez-Vargas et al. (2018) also reported the fitness of their experimental data to Freundlich isotherm, whereas other studies corroborate with the Langmuir isotherm model as also obtained in this research.

Adsorption Kinetics of Mn Fe, Pb and Cu ions from mining wastewater onto AAC and TiO$_2$-AAC.

The results of the kinetics of Mn (II), Fe (III), Cu (II) and Pb (II) ions adsorption onto AAC and TiO$_2$–AAC using PFO, PSO, Intra-particle Diffusion and Elovich Kinetics models are presented in Table 5. From the table,

Table 5 Kinetics parameters for AMD ions adsorption onto AAC and TiO$_2$–AAC

Parameters	AAC				TiO$_2$–AAC			
	Mn (II)	Fe (III)	Pb (II)	Cu (II)	Mn (II)	Fe (III)	Pb (II)	Cu (II)
Pseudo first order								
R^2	0.9237	0.5188	0.8836	0.875	0.7202	0.8555	0.5117	0.9022
K_1 (g/mg/min)	0.0304	0.0325	0.0308	0.0619	0.0249	0.0481	0.0456	0.042
$q_{e,exp}$ (mg/g)	0.8162	3.999	0.189	0.0186	0.8272	4.0026	0.195	0.037
$q_{e,cal}$ (mg/g)	0.1306	0.1362	0.0166	0.449	0.8296	4.0032	0.2022	0.0375
SSE	0.4851	14.920	0.0317	0.1703	0.6201	10.873	0.0136	0.0042
X^2	3.7139	109.51	1.905	0.3787	21.595	15.4208	0.0447	0.0501
Pseudo second order								
R^2	0.9999	1	0.9967	0.9930	0.9987	1	0.9998	0.8172
K_2 (g/mg/min)	1.6569	2.1971	0.7396	8.1803	0.2566	1.9363	3.0172	1.1580
$q_{e,exp}$ (mg/g)	0.8162	3.999	0.189	0.0186	0.8272	4.0026	0.195	0.037
$q_{e,cal}$ (mg/g)	0.8296	4.0032	0.2022	0.0375	0.8335	4.0048	0.189	0.018
SSE	5.76E−06	1.76E−05	5.24E−05	3.08–07	0.0137	0.0004	3.6E−05	0.0002
X^2	6.943E−06	4.41E−06	2.59E−04	8.22E−06	0.0165	9.993E−05	0.00019	0.0105

Parameters	AAC				TiO$_2$–AAC			
	Mn	Fe	Pb	Cu	Mn	Fe	Pb	Cu
Intraparticle								
R^2	0.5607	0.5437	0.7814	0.664	0.6928	0.5406	0.6192	0.9634
K_{int} (g/mg/min)	0.0468	0.2247	0.0128	0.0022	0.0503	0.2242	0.0111	0.0015
$q_{e,exp}$ (mg/g)	0.8162	3.999	0.189	0.0186	0.8272	4.0026	0.195	0.037
C (mg/g)	0.333	1.654	0.053	0.013	0.268	1.660	0.070	0.001
SSE	0.244	5.500	0.020	0.001	0.313	5.469	0.015	0.001
X^2	0.733	3.326	0.384	0.046	1.171	3.293	0.223	1.638

Parameters	AAC				TiO$_2$–AAC			
	Mn (II)	Fe (III)	Pb (II)	Cu (II)	Mn (II)	Fe (III)	Pb (II)	Cu (II)
Elovic								
R^2	0.816	0.828	0.962	0.901	0.973	0.824	0.957	0.759
α (g/mg/min^2)	1.836	0.366	0.052	0.013	10.143	1.068	0.028	0.002
β (g/mg/min)	1.361	6.583	26.455	144.927	6.139	1.358	25.381	178.57
$q_{e,cal}$ (mg/g)	0.673	0.133	0.012	0.004	0.674	0.274	0.013	0.005
SSE	0.023	14.941	0.033	0.001	0.024	13.876	0.043	0.002
X^2	0.035	11.746	2.640	0.242	0.035	50.641	3.328	0.342

coefficient of regression (R^2) values for the PSO model of Mn (II), Fe (III) and Cu (II) ions were closer to unity compared with the other models. Also, lower SSE and (X^2) error values obtained for the PSO model specify noteable agreement between the experimental ($q_{e,\exp}$) and the calculated ($q_{e,\exp}$) adsorption capacity results. Furthermore, the PSO model gave a higher rate constant (k_2) value than the PSO rate constant (k_1), which signifies a fast adsorption rate at the early contact time. The results obtained, therefore, suggest that the mechanism of adsorption of Mn (II), Fe (III) and Cu (II) ions from mining wastewater is PSO kinetics controlled, which is a chemisorption phenomenon driven. On the contrary, the Pb (II) ions adsorption from the mining wastewater onto the AAC and TiO_2–AAC adsorbent was better explained using the intraparticle diffusion model as a result of its high value of R^2 (0.933). The lower SSE and X^2 show a good correlation between the experimental ($q_{e,\exp}$) and the calculated ($q_{e,\exp}$) adsorption capacity with this model. The q_e values obtained for AAC are higher than the value obtained when natural clay was used by Khan et al. (2019) and Mustapha et al. (2019). This confirms that the AAC adsorbent is more efficient than other clays reported in the literature (Khan et al., 2019; Mustapha et al. 2019). The obtained PSO model agrees with several reported adsorption studies on TiO_2 composites (Kris Tri et al. 2019; Morsy 2017; Nouh et al. 2019).

Adsorption thermodynamics

The thermodynamic parameters of Mn (II), Fe (III), Pb (II) and Cu (II) ions adsorption onto the AAC and TiO_2-AAC adsorbents are displayed in Table 6. From Table 6, the value of ΔG° results at 313, 323, 333, 343 and 353 K were negative. The negative values imply that the adsorption of Mn (II), Fe (III), Pb (II) and Cu (II) ions onto the AAC and TiO_2–AAC adsorbents were both feasible and spontaneous (Egbosiuba et al. 2019). The change in enthalpy (ΔH°) positive values shows that the adsorption process is endothermic (Ogbu et al. 2019). More so, the enthalpy values obtained for Mn (II), Fe (II) and Cu (II) ions was greater than 40 kJ/mol (Miyah et al. 2017), implying that the reaction between the adsorbent and the adsorbate solution was chemically controlled (chemisorption), while enthalpy values for Cu (II) ions deviated from that of previous. (Khulbe and Matsuura 2019). The negative values obtained for entropy change (ΔS) for the adsorption of Mn (II), Fe (III), Cu (II) and Pb (II) ions onto the AAC and TiO_2–AAC suggest a reduction in the degree of randomness at the adsorbent/adsorbate interface during the adsorption process.

Table 6 Thermodynamics parameters for Mn, Fe, Cu and Pb ions adsorption from mining wastewater onto AAC and TiO_2–AAC

Temp (K)	Mn			Fe			Cu			Pb		
	ΔG° (kJ/mol)	ΔH° (kJ/mol)	ΔS° (J/mol)	ΔG° (J/mol)	ΔH° (kJ/mol)	ΔS° (J/mol)	ΔG° (J/mol)	ΔH° (kJ/mol)	ΔS° (J/mol)	ΔG° (J/mol)	ΔH° (kJ/mol)	ΔS° (J/mol)
AAC												
303	−4218.61	135.39	−0.43469	−14,071.7	89.250	−3.693	1418.73	132.200	−48.18	6705.3	3.318	−0.044
313	−4218.61			−9806.19			6117.714			6714.0		
323	−4206.53			−3255.4			9718.33			7814.784		
333	−3167.23			−2226.18			1345.04			9323.836		
343	−3146.4			−1870.29			919.87			8327.16		
AAC–TiO₂												
303	−3382.28	657.20	−3.353	−20,895.4	94.563	−1.11679	−257.86	88.012	−295.205	7576.97	17.082	−77.1913
313	−8020.61			−13,786.8			−312.15			8268.18		
323	−9078.77			−13,521.9			620.63			8716.76		
333	−12,055.4			−9740.08			1209.97			9254.71		
343	−14,149.2			−8516.15			6915.34			9677.99		

Comparison of adsorption parameters of AAC and TiO$_2$–AAC with literature

Table 7 shows the comparison of adsorption parameters of AAC and TiO$_2$–AAC for Pb (II), Cu (II), Mn (II) and Fe (III) ions, with the available data in the literature. For the adsorption of the Mn (II) ion, it was observed that TiO$_2$–AAC (89.34%) performed better than the AAC (83.12%). This may be due to the modification of the AAC by TiO$_2$ nanoparticles. However, Motsi et al. (2009) found that Zeolite removes Mn (II) ions more efficiently (95.20%) than both the AAC and TiO$_2$–AAC, although at a higher contact time of 360 min. This corroborates the findings of Marque et al. (2013) which revealed that the manganese removal increased with the increase in contact time until it reaches equilibrium. As shown in the table, all other adsorbents have a low efficiency of below 50% for Mn (II) ion removal. This justifies that the adsorbents in this study were efficient for the removal of Mn (II) ion at a lesser contact time of 120 min than that of the Zeolite (360 min). Also, both the AAC and TiO$_2$–AAC absorbents effectively remove Fe (III) ion from the mining wastewater at 86.45 and 91.99%, respectively, however, TiO$_2$–AAC performed better. Other adsorbents shown in the table such as zeolite, Ha–TiO$_2$ and cellulosic waste gave adsorbent efficiency of 59.5, 14.80 and 8.70%, respectively, for Fe (III) ion removal, which are below the values obtained in this study. The adsorption efficiency of Cu (II) unto AAC and TiO$_2$–AAC as shown in the table was 68.47 and 81.94%, respectively. This shows that the AAC and TiO$_2$–AAC removed Cu (II) ions from the wastewater more efficiently than some adsorbents reported in the literature (Budsaereechai et al. 2012; Sdiri et al. 2014). However, some other adsorbents such as anatase–rutile TiO$_2$ and anatase–rutile TiO$_2$-clay performed more efficiently than those investigated in this study, as shown in the table (Georgaka and Spanos 2010; Guillaume et al. 2018). This may be due to the surface area of respective adsorbents obtained from different clay sources. In addition, the contact time of the adsorption process could also be responsible for the increase in the removal percentage of Cu (II) ion as Guillaume et al. (2018) attained higher percentage removal of 91.19% Cu (II) ion at 240 min as against 120 min in this study. Therefore, the shorter contact time to remove Cu (II) ion indicate the efficacy of the adsorbents (AAC and TiO$_2$–AAC) investigated in this study. As the contact time plays a vital role in the adsorption process, which implies that a shorter interaction time in attaining equilibrium adsorption reduces the operational cost and the operating time (Rudi et al. 2020). From the table, Pb (II) ion was the least adsorbed compare to other heavy metals, as the AAC and TiO$_2$–AAC removed 29.48% and 32.39%, respectively. This is due to ionic radii of Pb (II) ion (0.119 nm) which is more than those of Fe (III) (0.060 nm), Mn (II) (0.070 nm) and Cu (II) (0.073 nm) ions. As the Pb (II) ion has the least chance to be incorporated into AAC and TiO$_2$-AAC structures compared with cations with smaller ionic radii (Mobasherpour et al., 2012). Generally, the TiO$_2$–AAC adsorbent revealed greater efficiency for the adsorption process as it was able to sequester multi ions from the mining wastewater in the order of Fe (III) > Mn (II) > Cu (II) > Pb (II). This is possible due to the improved surface area of the TiO$_2$–AAC adsorbent by the rutile-TiO$_2$ nanoparticle. Worthy of note is that the TiO$_2$–AAC adsorbent removed multi ions from the mining wastewater efficiently compared to other similar adsorbents identified in the table, hence, the novelty of this study.

Adsorption mechanism of AAC and TiO$_2$–AAC

Usually, mechanism of the heavy metal ions adsorption onto the nano adsorbents is greatly influenced by the surface chemistry of the adsorbent, the ionic charge on the metal ions and the adsorbate interactions (Miyah et al. 2017). From this research, the adsorption of Mn (II), Fe (III), Pb (II) and Cu(II) ions onto AAC and TiO$_2$-AAC was reliant on on the pH and ionic strength. Figure 11 provides information about the mechanism of the metal ions adsorption onto the two adsorbents. It can be seen that adsorption of heavy metal ions onto AAC and TiO$_2$–AAC was favoured by low pH (pH > pH$_{PZC}$) values below 8.0 for AAC and values below 10.0 for TiO$_2$–AAC point of zero charges, which resulted in the high amount of Mn (II), Fe (III), and Pb (II) ions adsorbed.

This was attributed to the strong intermolecular electrostatic attraction between the negatively charged adsorbate in mining wastewater and the positively charged AAC and TiO$_2$–AAC surface.

Nevertheless, at higher pH(pH > pH$_{PZC}$) (> 8 for AAC and > 10 for TiO$_2$–AAC), limited number of metal ions was adsorbed by AAC and TiO$_2$–AAC due to increase electronegativity (pH) of the adsorbate solution at the surface of the adsorbents. This reduces the susceptibility of the positive metal ions (Mn (II), Fe (III), Pb (II) and Cu (II)) adsorption because of electrostatic repulsion (Egbosiuba et al. 2019). Other adsorption mechanisms such as; ion exchange or hydrophobic bonding instead of electrostatic interactions may also be responsible for the heavy metal adsorption onto the AAC and TiO$_2$–AAC surface.

Conclusion

Rutile-titanium dioxide nanoparticles were successfully synthesised via the green synthesis method, using the aqueous leaf extract of *Parkia biglobossa*. The TiO$_2$ was anchored on acid-activated kaolinite clay and subjected to comparative

Table 7 Adsorption parameters of AAC, TiO$_2$–AAC and other adsorbents in literature

Adsorbents	TiO$_2$ Precursors	TiO$_2$ Phase	Initial conc. C$_o$(mg/L)	Contact Time (min)	Adsorbent Dosage (g)	Surface area m^2/g	Crystallite size (nm)	Efficiency (%)	References
Mn (II)									
Ha–TiO$_2$	TiCl$_4$	Anatase	300	15	0.05	449	–	24.92	Kanna et al. (2005)
Zeolite	Clinoptilolite	–	400	360	3.7	–	–	95.20	Motsi et al. (2009)
Graphene–Zinc oxide Nps	–	–	10.5	20	25.06	–	–	34.10	Leiva et al. (2021)
White rice husk	Organic	–	100	480	2.5	–	50,000	26.60	Tavlieva et al. (2015)
AAC	–		0.943	120	0.5	14.15	8.10	83.12	**This study**
TiO$_2$–AAC	–		0.943	120	0.5	32.98	6.11	89.34	**This study**
Fe (III)									
Zeolite	Clinoptilolite	–	400	360	3.7	–	–	59.50	Motsi et al. (2009)
Ha–TiO$_2$	TiCl$_4$	Anatase	300	15	0.05	449	–	14.80	Kanna et al. (2005)
Cellulosic waste	Organic materials	–	4000	1440	2	2.66	–	8.70	Genty et al. (2017)
AAC	–		20.02	120	0.5	14.15	8.10	86.45	**This study**
TiO$_2$–AAC	–		20.02	120	0.5	32.98	6.11	91.99	**This study**
Cu (II)									
Ag/Ti/clay	–		200	–	–	–	–	97.50	Ajenifuja et al. (2016)
Clay–TiO$_2$	TiO$_2$	A–R	100	240	0.1	50	30	91.19	Guillaume et al. (2018)
Raw clay	–	–	1000	60	1	17.84	–	3.07	Sdiri et al. (2014)
Bentonite	–		10	60	0.5	–	–	76.88	Hussain and Ali (2021)
TiO$_2$	TIO$_2$	A–R	1.28	30	0.5	50	30	99.90	Georgaka and Spanos (2010)
Raw clay	Bentonite	–	2000	864	1	47	–	25.40	Budsaereechai et al. (2012)
Ag/Ti/clay	–		1000	288	0.12	–	–	91.50	Ajenifuja et al. (2016)
Activated clay	–		2000	864	1	74	–	29.97	Budsaereechai et al. (2012)
AAC	–		0.943	120	0.5	14.15	8.10	68.47	**This study**
TiO$_2$–AAC	–		0.943	120	0.5	32.98	6.11	81.94	**This study**
Pb (II)									
LAO–TiO$_2$	TiCl$_4$		50.00	1440	0.25	–	–	4.40	Bijang 2020
Bentonite	Local		10	60	0.5	–	–	75.76	Hussain and Ali (2021)
Raw clay	Bentonite	–	2000	864	1	47	–	76.50	Budsaereechai et al. (2012)
Activated clay	–		2000	864	1	74	–	84.00	Budsaereechai et al. (2012)
AAC	Kaolin		0.94	120	0.5	32.98	8.10	29.48	**This study**
TiO$_2$–AAC	TTIP		0.94	120	0.5	32.98	6.11	32.39	**This study**

They are for emphasis, referring to the present study
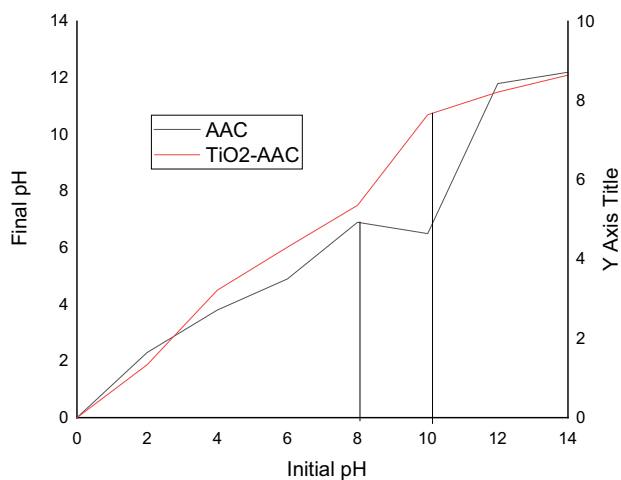
Fig. 11 pH point of zero charges of AAC and TiO$_2$–AAC

adsorptive studies with ordinary activated kaolinite clay for the removal of selected heavy metals from mining wastewater. The characterisation study established that the AAC and TiO$_2$–AAC are porous adsorbents for the removal of Mn (II), Fe (III), Pb (II) and Cu (II) ions from the mining wastewater, with TiO$_2$–AAC surface more porous than the AAC, due to its modification by TiO$_2$. TiO$_2$–AAC has a smaller crystallite size of 6.11 nm adjudged better than AAC with 8.10 nm crystallite size. The BET surface area of the adsorbents was also increased from 14.15 m^2/g (AAC) to 32.98 m^2/g (TiO$_2$–AAC). The synthesised and the anchored titanium was stable in the $+4$ oxidation state as revealed by the XPS characterisation. Finest conditions for the removal of the four ions under the applied conditions of 120 min with 0.5 g adsorbent dose and 70 °C were; 83.45% Mn (II), 86.13% Fe (III), 68.47% Cu (II) and 29.39% Pb (II) by AAC and 89.36% Mn (II), 91.99% Fe (III), 81.94% Cu (II) with 32.39% Pb (II) by TiO$_2$–AAC. The adsorption of heavy metal ions was also discovered to depend on the ionic strength, surface area and surface functional groups of the adsorbents. The adsorption isotherm and kinetic model showed good agreement with Langmuir and pseudo-second-order model for both AAC and TiO$_2$–AAC. The thermodynamic parameters confirmed a spontaneous, feasible, less random and chemisorption adsorption process by the adsorbents. The anchoring of TiO$_2$ nanoparticles onto acid-treated kaolinite clay enhanced the percentage removal of the unwanted heavy metals from the mining wastewater compared to AAC alone.

Declarations

Conflicts of interest There is no conflict of interest.

Ethics approval Not applicable.

Consent for publication All the authors agreed to submit the manuscript in this journal.

References

Abdallah S (2019) Remediation of copper and zinc from wastewater by modified clay in Asir region southwest of Saudi Arabia. Open Geosci 11:505–512. https://doi.org/10.1515/geo-2019-0041

Abu-Dalo M, Jaradat A, Albiss BA, Al-Rawashdeh NAF (2019) Green synthesis of TiO2 NPs/pristine pomegranate peel extract nanocomposite and its antimicrobial activity for water disinfection. J Environ Chem Eng. https://doi.org/10.1016/j.jece.2019.103370

Abunah D, Onindo C, Andala D, Ochoti E (2019) Physico-chemical removal of heavy metals from contaminated water using recyclable montmorillonite cellulose nanocomposite. J Mater Environ Sci 10(12):1349–1361

Acheampong MA, Ansa EDO (2017) Low-cost technologies for mining wastewater treatment. J Environ Sci Eng B(6):391–405. https://doi.org/10.17265/2162-5263/2017.08.001

Ahamed MI, Inamuddin L, Sharma G, Khan A, Asiri AM (2016) Turmeric/polyvinyl alcohol Th(IV) phosphate electrospun fibers: synthesis, characterization and antimicrobial studies. J Taiwan Inst Chem Eng 68:407–414. https://doi.org/10.1016/j.jtice.2016.08.024

Ajenifuja E, Ajao JA, Ajayi EOB (2016) Equilibrium adsorption isotherm studies of Cu (II) and Co (II) in high concentration aqueous solutions on Ag–TiO2-modified kaolinite ceramic adsorbents. Appl Water Sci. https://doi.org/10.1007/s13201-016-0403-6

Akinnawo S (2019) Synthesis, modification, applications and challenges of titanium dioxide nanoparticles. Res J Nanosci Eng 3(14):10–22

Alaya-Ibrahim S, Kovo AS, Abdulkareem AS, Adeniyi OD, Yahya MD (2019) Development of nano-silver doped zeolite asynthesized from Nigerian Ahoko kaolin for treatment of wastewater of a typical textile company. Chem Eng Commun 9:1–25. https://doi.org/10.1080/00986445.2019.1641490

Al-Essa K, Khalili F (2018) Heavy metals adsorption from aqueous solutions onto unmodified and modified jordanian kaolinite clay: batch and column techniques. Am J Appl Chem 6(1):25

Ashraf S, Siddiqa A, Shahida S, Qaisar S (2019) Titanium-based nano-composite materials for arsenic removal from water: a review. Heliyon 5(01577):1–8. https://doi.org/10.1016/j.heliyon.2019.e01577

Ayawei N, Ebelegi AN, Wankasi D (2017) Modelling and interpretation of adsorption isotherms. J Chem 2017:3039817. https://doi.org/10.1155/2017/3039817

Balali-Mood M, Naseri K, Tahergorabi Z, Khazdair MR, Sadeghi M (2021) Toxic mechanisms of five heavy metals: mercury. Lead, Chromium, Cadmium, and Arsenic. https://doi.org/10.3389/fphar.2021.643972

Bankole MT, Abdulkareem AS, Mohammed IA, Ochigbo SS, Tijani JO, Abubakre OK, Roos WD (2019) Selected heavymetals removal from electroplating wastewater by purifiedand polyhydroxylbutyrate functionalized carbon nanotubesadsorbents. Sci Rep 9:1–19. https://doi.org/10.1038/s41598-018-37899-4

Bhateria R, Singh R (2019) A review on nanotechnological application of magnetic iron oxides for heavy metal removal. J Water Process Eng. https://doi.org/10.1016/j.jwpe.2019.100845

Bijang CM, Nurdin M, Azis T, Sekewael SJ, Wattimena H (2020) ouw natural clay-titanium Oksida (LaO-TiO2) composite adsorption ability on lead (Pb) metal. J Phys Conf Ser 1463:012011

Bok-Badura J, Jakóbik-Kolon A, Karoń K, Mitko K (2018) Sorption studies of heavy metal ions on pectin-nano-titanium dioxide composite adsorbent. Sep Sci Technol 53(7):1034–1044. https://doi.org/10.1080/01496395.2017.1329840

Boparai HK, Joseph M, O'Carroll DM (2011) Kinetics and thermodynamics of cadmium ion removal by adsorption onto nano zerovalent iron particles. J Hazard Mater 186(1):458–465

Budsaereechai S, Kamwialisak K, Ngernyen Y (2012) Adsorption of lead, cadmium and copper on natural and acid activated bentonite clay. KKU Res J 17(5):800–810

Bwapa JK, Jaiyeola AT, Chetty R (2017) Bioremediation of acid mine drainage using algae strains: a review. S Afr J Chem Eng 24:62–70

Cardoso BN, Kohlrausch EC, Laranjo MT, Benvenutti EV, Balzaretti NM, Arenas LT, Costa TMH (2019) Tuning anatase-rutile phase transition temperature: TiO2/SiO2 nanoparticles applied in dye-sensitized solar cells. Int J Photoenergy 2019:1–9. https://doi.org/10.1155/2019/7183978

Dedehou VF, Olounladé PA, Adenilé DA, Alowanou G, Azando EV, Hounzangbé-Adoté MS (2016) A review on medicinal plants of Parkia Biglobosa (*Mimosaceae–Fabaceae*) and *Pterocarpus Erinaceus* (*Leguminosae–Papilionoidea*). J Med Plants 4(6):132–137

Dubinin MM (1969) The potential theory of adsorption of gastheory of adsorption of gases and vapour. Chem Rev 60:235–241

Durango-Giraldo G, Cardona A, Zapata JF, Santa JF, Buitrago-Sierra R (2019) Titanium dioxide modified with silver by two methods for bactericidal applications. Heliyon 5(5):e01608

Egbosiuba TC, Abdulkareem AS, Kovo AS, Afolabi EA, Tijani JO, Auta M, Roos WD (2019) Ultrasonic enhanced adsorption of methylene blue onto the optimized surface area of activated carbon: adsorption isotherm, kinetics and thermodynamics. Chem Eng Res Des 153:315–336

Esmaeili A, Mobini M, Eslami H (2019) Removal of heavy metals from acid mine drainage by native natural clay minerals, batch and continuous studies. Appl Water Sci 9(97):1–6. https://doi.org/10.1007/s13201-019-0977-x

Falk GS, Borlaf M, López-Muñoz MJ, Fariñas JC, Rodrigues Neto JB, Moreno R (2018) Microwave-assisted synthesis of TiO2 nanoparticles: photocatalytic activity of powders and thin films. J Nanopart Resour 20(23)

Fu W, Chen H, Yang S, Huang W, Huang Z (2019) Poly(-diallyldimethylammonium-MoS4) based amorphous molybdenum sulphide composite for selectively mercury uptake from wastewater

across a large pH region. Chemosphere 232:9–17. https://doi.org/10.1016/j.chemosphere.2019.05.182

Genty T, Bussière B, Benzaazoua M, Neculita CM, Zagury GJ (2017) Iron removal in highly contaminated acid mine drainage using passive biochemical reactors. Water Sci Technol 76(7):1833–1843. https://doi.org/10.2166/wst.2017.362

Georgaka A, Spanos N (2010) Study of the cu (II) removal from aqueous solutions by adsorption on titania. Global NEST J 12(3):239–247

Gholipour A, Zahabi H, Stefanakis AI (2020) A novel pilot and full-scale constructed wetland study for glass industry wastewater treatment. Chemopshere. https://doi.org/10.1016/j.chemosphere.2020.125966

Guillaume PLA, Chelaru A, Visa M, Lassiné O (2018) Titanium oxide-clay" as adsorbent and photocatalysts for wastewater treatment. J Membr Sci Technol 8(1):176–186. https://doi.org/10.4172/2155-9589.1000176

Guo H, Wang W, Liu L, He Y, Li C, Wang Y (2013) Shape-controlled synthesis of Ag@TiO2 cage-bell hybrid structure with enhanced photocatalytic activity and superior lithium storage+. Green Chem 15:2810–2816. https://doi.org/10.1039/c3g41280f

Ho YS, McKay G (1999) Pseudo-second order model for sorption processes. Process Biochem 34(5):451–465. https://doi.org/10.1016/S0032-9592(98)00112-5

Hussain ST, Ali SAK (2021) Removal of heavy metal by ion exchange using bentonite clay. J Ecol Eng 22(1):104–111. https://doi.org/10.12911/22998993/128865

Kamal NA, Gooyong L (2019) Removal of selected heavy metals in acid mine drainage using chemical precipitation method. J Adv Res Fluid Mech Therm Sci 57(1):121–130

Kanna M, Wongnawa W, Sherdshoopongse P, Boonsin P (2005) Adsorption behavior of some metal ions on hydrated amorphous titanium dioxide surface. Songklanakarin J Sci Technol 27(5):1017–1026

Kefeni KK, Msagati TAM, Mamba BB (2017) Acid mine drainage: prevention, treatment options, and resource recovery: a review. J Clean Prod 151(2017):475–493

Kenne-Diffo B, Elimbi A, Cyr M, Dika-Manga J, Tchakoute KH (2015) Effect of the rate of calcination of kaolin on the properties of metakaolin-based geopolymers. J Asian Ceram Soc 3(1):130–138

Khan MI, Almesfer MK, Danish M, Ali IH, Shoukry H, Patel R, Rehan M (2019) Potential of Saudi natural clay as an effective adsorbent in heavy metals removal from wastewater. Desalin Water Treat 158:140–151. https://doi.org/10.5004/dwt.2019.24270

Khulbe KC, Matsuura T (2019) Removal of heavy metals and pollutants by membrane adsorption techniques. Appl Water Sci 8(19):1–30. https://doi.org/10.1007/s13201-018-0661-6

Kris Tri B, Lutfi Aditya H, Elza J (2019) Adsorption of uranium simulation waste using bentonite:titanium dioxide. Urania 25(1):19–31

Krishnan B, Mahalingam S (2017) Ag/TiO2/bentonite nanocomposite for biological applications: synthesis, characterization, antibacterial and cytotoxic investigations. Adv Powder Technol 28:2265–2280. https://doi.org/10.1016/j.apt.2017.06.007

Lakherwal D (2014) Adsorption of heavy metals: a review. Int J Environ Res Develop 4(1):41–48

Landage KS, Arbade GK, Khanna P, Bhongale CJ (2020) Biological approach to synthesize TiO2 nanoparticles using Staphylococcus aureus for antibacterial and anti-biofilm applications. J Microbiol Exper 8(1):36–43. https://doi.org/10.15406/jmen.2020.08.00283

Langmuir I (1918) The constitution and fundamental properties of solids and liquids. J Am Chem Soc 38:2221–2295

Leiva E, Tapia C, Rodríguez C (2021) Removal of Mn(II) from acidic waste waters using graphene oxide—Zno nanocomposites. Molecules 26(2713):1–18. https://doi.org/10.3390/molecules26092713

Li L, Yan J, Wang T, Zhao Z, Gong J, Guan N (2015) Sub-10 nm rutile titanium nanoparticles for efficient visible-light-driven photocatalytic hydrogen production. Nat Commun. https://doi.org/10.1038/ncomms6881

Liu T, Liu Z, Zhang R, Wang Y, Bruggen B, Wang X (2015) Fabricationofathin film nanocompositehollow fiber nanofiltration membrane for wastewater treatment. J Membr Sci 488:92–102. https://doi.org/10.1016/j.memsci.2015.04.020

Madadi Z, Soltanieh M, Lotfabad TB, Nazari BS (2020) Green synthesis of titanium dioxide nanoparticles with Glycyrrhiza glabra and their photocatalytic activity. Asian J Green Chem 4(3):256–268. https://doi.org/10.33945/SAMI/AJGC.2020.3.3

Madzivire G, Gitari WM, Vadapalli VRK, Ojumu TV, Petrik LF (2011) Fate of sulphate removed during the treatment of circumneutral mine water and acid mine drainage with coal fly ash: Modelling and experimental approach. Miner Eng 24:1467–1477

Malima N, Lugwisha E, Mwakaboko A (2018) The efficacy of raw Malangali kaolin clay in the adsorptive removal of cadmium and cobalt ions from water. Tanzania J Sci 44(2):64–30

Manisalidis I, Stavropoulou E, Stavropoulos A, Bezirtzoglou E (2020) Environmental and health impacts of air pollution: a review. Front Public Health. https://doi.org/10.3389/fpubh.2020.00014

Marque TL, Alves VN, Coelho LM, Coelho NMM (2013) Assessment of the use of Moringa oleifera seeds for removal of manganese ions from aqueous systems. BioResources 8:2738–2751

Martinez-Vargas S, Martínez AI, Hernandez-Beteta EE, Mijangos-Ricardez OF, Vazquez-Hipolito V, Patino-Carachure C, Lopez-Luna J (2018) As(III) and As(V) adsorption on manganese ferrite nanoparticles. J Mol Struct 1154:524–534. https://doi.org/10.1016/j.molstruc.2017.10.076

Masindi V, Muedi KL (2018) Heavy metals. In: Saleh HEDM, Aglan RF (Eds.), Environmental contamination by heavy metals. Accepted from https://www.intechopen.com/books/heavy-metals/environmental-contamination-by-heavy-metals. https://doi.org/10.5772/intechopen.76082

Miyah Y, Lahrichi A, Idrissi M, Boujraf S, Taouda H, Zerrouq F (2017) Assessment of adsorption kinetics for removal potential of Crystal Violet dye from aqueous solutions using Moroccan pyrophyllite. J Assoc Arab Univ Basic Appl Sci 23:20–28. https://doi.org/10.1016/j.jaubas.2016.06.001

Mobasherpour I, Salahi E, Pazouki M (2012) Comparative of the removal of Pb^{2+}, Cd^{2+} and Ni^{2+} by nano crystallite hydroxyapatite from aqueous solutions: Adsorption isotherm study. Arab J Chem 5:439–446. https://doi.org/10.1016/j.arabjc.2010.12.022

Morsy AMA (2017) Performance of magnetic talc titanium oxide composite for thorium ions adsorption from acidic solution. Environ Technol Innov 8:399–410. https://doi.org/10.1016/j.eti.2017.09.004

Motsi T, Rowson NA, Simmons MJH (2009) Adsorption of heavy metals from acid mine drainage by natural zeolite. Int J Miner Process 92(2009):42–48. https://doi.org/10.1016/j.minpro.2009.02.005

Mungondori HH, Mtetwa S, Tichagwa L, Katwire TM, Nyamukamba P (2017) Synthesis and application of a ternary composite of clay, saw-dust and peanut husks in heavy metal adsorption. Water Sci Technol 12(3):1–11. https://doi.org/10.2166/wst.2017.123

Musial J, Krakowiak R, Mlynarczyk DT, Goslinski T, Stanisz BJ (2020) Titanium dioxide nanoparticles in food and personal care products—What do we know about their safety? Nanomaterials 10(6):1110–1121

Mustapha S, Ndamitso MM, Abdulkareem AS, Tijani JO, Mohammed AK, Shuaib DT (2019) Potential of using kaolin as a natural adsorbent for the removal of pollutants from tannery wastewater. Heliyon 5(e02923):1–17. https://doi.org/10.1016/j.heliyon.2019.e02923

Mustapha S, Ndamitso MM, Abdulkareem AS, Tijani JO, Shuaib DT, Ajala AO, Mohammed AK (2020) Application of TiO_2 and

ZnO nanoparticles immobilized on clay in wastewater treatment: a review. Appl Water Sci 10(49):1–36. https://doi.org/10.1007/s13201-019-1138-y

Nigerian Industrial Standard (NIS) (2015) Nigerian Standard for Drinking Water Quality. https://africacheck.org/wpcontent/uploads/2018/06/Nigerian-Standard-for-Drinking-Water-Quality-NIS-554-2015.pdf

Nouh EA, Lasheen TA, El-sherif RM, Abdel-Ghany NA (2019) CeO_2–$TiFe_2O_4$ nanocomposite for efective removal of uranium ions from aqueous waste solutions. Springer Nature Appl Sci 1(159):1–13

Oh WD, Wong Z, Chen X, Lin KYA, Veksha A, Lisak G, Lim TT (2020) Enhanced activation of peroxydisulfate by CuO decorated on hexagonal boron nitride for bisphenol a removal. Chem Eng J. https://doi.org/10.1016/j.cej.2020.124714

Ojonimi T, Asuke F, Onimisi M, Onuh C (2019) Acid mine drainage (AMD): an environmental concern generated by coal mining. J Degr Mining Lands Manag 6:1875–1881. https://doi.org/10.15243/jdmlm.2019.064.1875

Ouyang D, Zhuo Y, Hu L, Zeng Q, Hu Y, He Z (2019) Research on the adsorption behavior of heavy metal ions by porous material prepared with silicate tailings. Minerals 9(291):1–16. https://doi.org/10.3390/min9050291

Patidar V, Jain P (2017) Green synthesis of TiO2 nanoparticle using moringa oleifera leaf extract. Int Res J Eng Technol 4(3):1–4

Pavesi T, Moreira JC (2020) Mechanisms and individuality in chromium toxicity in humans. J Appl Toxicol 40:1183–1197. https://doi.org/10.1002/jat.3965

Pietrelli L, Ippolito NM, Ferro S, Dovì VG, Vocciante M (2019) Removal of Mn and as from drinking water by red mud and pyrolusite. J Environ Manag 237:526–533. https://doi.org/10.1016/j.jenvman.2019.02.093

Prasse C, Stalter D, Schulte-Oehlmann U, Oehlmann J, Ternes T (2015) Spoilt for choice: a critical review on the chemical and biological assessment of current wastewater treatment technologies. Water Res 87:237–270

Redha A, Al-Hasan R, Afzal M (2021) Synergistic and concentration-dependent toxicity of multiple heavy metals compared with single heavy metals in conocarpus lancifolius. Environ Sci Pollut Res 28(18):23258–23272. https://doi.org/10.1007/s11356-020-12271-0

Rodríguez-Padrón D, Puente-Santiago AR, Luna-Lama F, Caballero AL, Muñoz-Batista MJ, Luque R (2019) Versatile protein-templated TiO_2 nanocomposite for energy storage and catalytic applications. ACS Sustain Chem Eng 7(5):5329–5337

Rudi NN, Muhamad MS, Chuan LT, Alipal J, Omar S, Hamidon N, Harun H (2020) Evolution of adsorption process for manganese removal in water via agricultural waste adsorbents. Heliyon. https://doi.org/10.1016/j.heliyon.2020.e05049

Saha S, Sinha A (2018) A review on treatment of acid mine drainage with waste materials: a novel approach. Global NEST J 20(3):512–528. https://doi.org/10.30955/gnj.002610

Sdiri AT, Higashi T, Jamoussi F (2014) Adsorption of copper and zinc onto natural clay in single and binary systems. Int J Environ Sci Technol 11:1081–1092. https://doi.org/10.1007/s13762-013-0305-1

Seo EY, Cheong YW, Yimb GJ, Mina KW, Geroni JW (2016) Recovery of Fe, Al and Mn in acid coal mine drainage by sequential selective precipitation with control of pH. CATENA 148:11–16. https://doi.org/10.1016/j.catena.2016.07.022

Shukla SK, Mushaiqri NR, Subhi HMA, Yoo K, Sadeq HA (2020) Low-cost activated carbon production from organic waste and its utilization for wastewater treatment. Appl Water Sci. https://doi.org/10.1007/s13201-020-1145-z

Siddiqui SI, Chaudhry SA (2017) Iron oxide and its modified forms as an adsorbent for arsenic removal: a comprehensive recent

advancement. Process Saf Environ Prot 111:592–626. https://doi.org/10.1016/j.psep.2017.08.009

Soni M, Mehta P, Soni A, Goswami GK (2018) Green nanoparticles: synthesis and applications. J Biotechnol Biochem 4(3):78–83. https://doi.org/10.9790/264X-0403017883

Subhapriya S, Gomathipriya P (2018) Green synthesis of titanium dioxide (TiO2) nanoparticles by Trigonella foenum-graecum extract and its antimicrobial properties. Microb Pathog 116:215–220. https://doi.org/10.1016/j.micpath.2018.01.027

Subhi HA, Adeeb MS, Pandey M, Sadeq HA, Kumar D, Shukla SK (2020) Effect of different activation agents on the pollution removal efficiency of date seed activated carbon: process optimization using response surface methodology. Appl Water Sci 10(166):1–9. https://doi.org/10.1007/s13201-020-01251-x

Swathi N, Sandhiya D, Rajeshkumar S, Lakshmi T (2019) Green synthesis of titanium dioxide nanoparticles using Cassia fistula and its antibacterial activity. Int J Res Pharm Sci 10(2):856–860. https://doi.org/10.26452/ijrps.v10i2.261

Tavlieva MP, Genieva SD, Georgieva VG, Vlaev LT (2015) Thermodynamics and kinetics of the removal of manganese(II) ions from aqueous solutions by white rice husk ash. J Mol Liq 211:938–947

Tijani JO, Momoh UO, Salau RB, Bankole MT, Abdulkareem AS, Roos WD (2019) Synthesis and characterization of $Ag_2O/B_2O_3/TiO_2$ ternary nanocomposites for photocatalytic mineralization of local dyeing wastewater under artificial and natural sunlight irradiation. Environ Sci Pollut Res. https://doi.org/10.1007/s11356-019-05124-y

Wang Z, Bao J, Wang T, Moryani HT, Kang W, Zheng J, Xiao W (2021) Hazardous heavy metals accumulation and health risk assessment of different vegetable species in contaminated soils from a typical mining city. Central China 18(5):2617

World Health Organization (WHO) (2017) Guidelines for drinking-water quality. Fourth Edition, Incorporating First Addendum, Volume 1 Recommendation, Geneva. ISBN: 9789241549950. http://www.who.int/water_sanitation_health/dwq/fulltext.pdf

Xiang Q, Ma X, Zhang D, Zhou H, Liao Y, Zhang H, Bazaka K (2019) Interfacial modification of titanium dioxide to enhance photocatalytic efficiency towards H_2 production. J Colloid Interface Sci 556:376–385

Xie Y, Lu G, Yang C, Qu L, Chen M, Guo C, Dang Z (2018) Mineralogical characteristics of sediments and heavy metal mobilization along a river watershed affected by acid mine drainage. PLoS ONE 13(1):1–17. https://doi.org/10.1371/journal.pone.0190010

Yang K, Liu Y, Li Y, Cao Z, Zhou C, Wang Z, Xu X (2019) Applications and characteristics of Fe–Mn binary oxides for Sb(V) removal in textile wastewater: selective adsorption and the fixed-bed column study. Chemosphere 232:254–263. https://doi.org/10.1016/j.chemosphere.2019.05.194

Youssef HF, Hegazy WH, Abo-almaged HH, El-Bassyouni GT (2015) Novel synthesis method of micronized Ti-zeolite Na-A and cytotoxic activity of its silver exchanged form. Bioinorg Chem Appl 2015:1–12. https://doi.org/10.1155/2015/428121

Yusof KN, Alias SS, Harun Z, Basri H, Azhar FH (2018) Parkia speciosa as reduction agent in green synthesis of silver nanoparticles. Chem Select 3:1–6

Zahir AA, Chauhan I, Bagavan A, Kamaraj C, Elango G, Shankar J, Singh N (2015) Green synthesis of silver and titanium dioxide nanoparticles using euphorbia prostrata. Antimicrob Agents Chemother 59(8):4782–4799

Zendelska A, Golomeova M, Golomeov B, Krstev B (2018) Effect of competing cations (Cu, Zn, Mn, Pb) adsorbed by Zeolite bearing Tuff from Macedonia. Nat Environ Pollut Technol 17(1):21–23

Zhao C, Ge R, Zhen Y, Wang Y, Li Z, Shi Y, Chen X (2019) A hybrid process of coprecipitation-induced crystallization-capacitive deionization-ion exchange process for heavy metals removal from hypersaline ternary precursor wastewater. Chem Eng J. https://doi.org/10.1016/j.cej.2019.122136